Seismic Imaging of Crust Beneath the Western Tibet-Pamir and Western Himalaya Using Ambient Noise and Earthquake Data

Vivek Kumar, Shyam S Rai, Rhys Hawkins, Thomas Bodin

JGR Solid Earth

RESEARCH ARTICLE
10.1029/2021JB022574

Seismic Imaging of Crust Beneath the Western Tibet-Pamir and Western Himalaya Using Ambient Noise and Earthquake Data

Vivek Kumar[1], Shyam S. Rai[1], Rhys Hawkins[2,3], and Thomas Bodin[3]

[1]Department of Earth and Climate Science, Indian Institute of Science Education & Research Pune, Pune, India, [2]Department of Earth Sciences, Utrecht University, Utrecht, The Netherlands, [3]ENSL, CNRS, LGL-TPE, University Lyon, University Lyon 1, Villeurbanne, France

Key Points:

- The northern limit of the Indian crust extends beyond the Qiangtang block in western Tibet and till the central Pamir farther in the west
- Laterally discontinuous mid-crustal low-velocity zones do not support the pervasive channel flow model
- The Karakoram Fault is an upper crustal feature extending to a depth of 20 km

Supporting Information:

Supporting Information may be found in the online version of this article.

Correspondence to:

V. Kumar,
vivek.seismology@gmail.com

Citation:

Kumar, V., Rai, S. S., Hawkins, R., & Bodin, T. (2022). Seismic imaging of crust beneath the western Tibet-Pamir and western Himalaya using ambient noise and earthquake data. *Journal of Geophysical Research: Solid Earth*, *127*, e2021JB022574. https://doi.org/10.1029/2021JB022574

Received 9 JUN 2021
Accepted 24 MAY 2022

Abstract We present a new high-resolution image of the crust beneath the western Himalaya-Asia convergence zone encompassing the geographical domain of western Himalaya-western Tibet-Ladakh-Karakoram-Pamir-Hindu Kush, using ambient noise cross-correlations from 530 seismological stations along with surface wave observations from 1,261 earthquakes recorded over the network. The 3-D shear wave velocity image is created using 22,726 inter-station Rayleigh wave dispersion measurements from 5 to 60 s period at a horizontal resolution of less than 0.5° × 0.5° following the Bayesian Trans-dimensional Tree tomography approach. The Moho beneath the Himalayas and south Tibet correlates with a velocity transition of 4.4–4.6 km/s and a reduced velocity transition of 4.0–4.2 km/s in northern Tibet and the Pamir. We used the Moho depth and the nature of high-velocity lower crust (Vs > 4.0 km/s) to map the northern limit of the Indian crust that extends beyond the Qiangtang block in western Tibet (77–82°E) from its previously assumed boundary in the Lhasa block and till the central Pamir farther west. The velocity image reveals discontinuous low-velocity zones (LVZs; Vs < 3.4 km/s) in the mid-crust of western Tibet and the Pamir that do not support the existence of the channel flow model. The LVZs in the Pamir correlate with the surface distribution of gneiss domes. The lowest velocities (Vs < 3.2 km/s) are observed over the Ladakh-Karakoram batholith and the Nanga Parbat region. The study suggests a continuation of LVZs across the Karakoram Fault at a depth below 20 km, indicating the fault's upper crustal depth extent.

Plain Language Summary The Tibetan plateau, the Himalayas, and the Pamir are the most spectacular products of the continued collision of the Indian plate with the Asian plate since about 60 Ma. To provide constraints on the geodynamic processes responsible for the creation of these features, we present a high-resolution 3-D shear velocity model of the underlying crust beneath the poorly studied western segment of the India-Asia collision zone. Using crustal thickness and the nature of the high-velocity lower crust, we map the underthrusted Indian crust extending close to the northern end of western Tibet, and till the central Pamir farther west. As a consequence of the underthrusting, the low viscosity Indian crust beneath Tibet was proposed to flow southward and extrude along the Himalayan front. We examine the validity of this "channel flow model". Our velocity model shows discontinuous low-velocity zones (LVZs) in the middle crust of western Tibet and the Pamir that do not support the presence of a pervasive channel flow, questioning the validity of the "channel flow model". In the Pamir, the LVZs correlate with gneissic domes. Our model also shows that the Karakoram Fault is a shallow crustal feature as it does not disrupt the mid-crustal LVZs.

1. Introduction

The Himalaya-Tibet-Pamir mountain belts (Figure 1) have an evolutionary history beginning about 60 Myr ago with the closure of the Tethys Ocean followed by the collision of the Eurasian and Indian landmass (An et al., 2021; Copley et al., 2010; DeCelles et al., 2014; Kapp & DeCelles, 2019; Molnar et al., 1993; Tapponnier et al., 2001; Yin & Harrison, 2000). Since the collision, India has moved northward ~2,000–3,600 km (Johnson, 2002; McKenzie & Sclater, 1971; Meng et al., 2020; Molnar & Tapponnier, 1975; Van Hinsbergen et al., 2011, 2012, 2019). A part of this convergence has been accommodated in the deformation of the northern margin of the Indian plate, and most estimates suggest that about 1,500–2,000 km of the convergence remains unaccounted for (England & Houseman, 1986; Johnson, 2002; Van Hinsbergen et al., 2011, 2012, 2019). This difference has been explained by the thrusting of the Indian continental lithosphere beneath Asia (Argand, 1924; Molnar & Tapponnier, 1975;

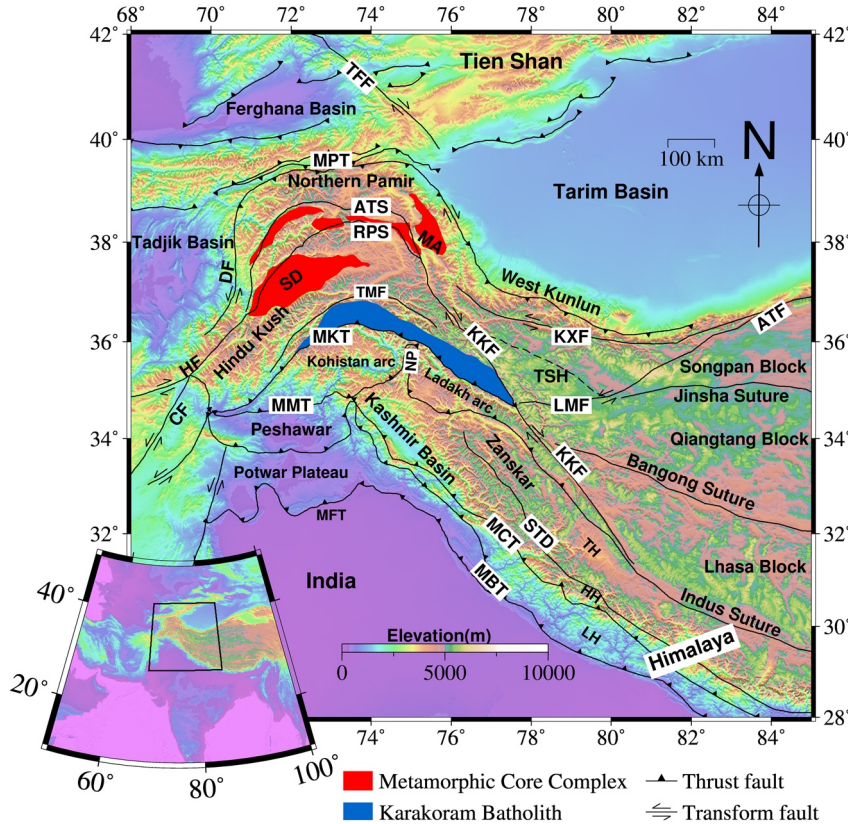

Figure 1. Topographic map of the study region that includes western Tibet-Himalaya, Ladakh-Kohistan arc, and the Pamir-Hindu Kush. Major tectonic blocks and faults are marked as black lines (Searle & Hacker, 2019; Yin & Harrison, 2000). The red shaded areas denote metamorphic core complexes (gneiss domes) of the Pamir. The blue shaded area is the Karakoram batholith. The black polygon in the inset image at the bottom left indicates the study region. SD, Shakhdara dome; MA, Muztagh Ata dome; MFT, Main Frontal Thrust; MBT, Main Boundary Thrust; MCT, Main Central Thrust; STD, Southern Tibetan Detachment; MMT, Main Mantle Thrust; LMF, Longmucuo Fault; TSH, Tianshuihai block; ATF, Altyn Tagh Fault; KXF, Karakax Fault; KKF, Karakoram Fault; MKT, Main Karakoram Thrust; NP, Nanga Parbat; TTF, Talas-Ferghana Fault; RPS, Rushan Pshart Suture; ATS, Akbaytal Tanymas Suture; MPT, Main Pamir Thrust; CF, Chaman Fault; HF, Herat Fault; DF, Darvaz Fault; TMF, Tirich Mir Fault; TH, Tethys Himalaya; HH, High Himalaya; LH, Lesser Himalaya.

Powell & Conaghan, 1973; Thatcher, 2007) and/or diffused deformation within Asia (Dewey & Burke, 1973; England & McKenzie, 1982; England & Molnar, 2005; P. Z. Zhang et al., 2004, reviewed by Jade et al. [2004] and Loveless and Meade [2011]). This process led to crustal thickening that uplifted the Himalayas and the Pamir-Tibetan Plateau. The crustal thickness increases from ~40 km beneath India and the southern edge of the Himalayas to ~60 km in the Higher Himalaya, ~70 km in Ladakh (and southern Tibet), and up to ~90 km beneath Tibet and the Pamir (Kufner et al., 2016; Priestley et al., 2019; Reguzzoni et al., 2013; Schneider et al., 2019). Farther north, beyond the Tibetan plateau, the crust thins due to the presence of rigid cratonic blocks of Asia, such as the Tarim Basin, Tadjik Basin, and Qaidam Basin (Kao et al., 2001; Q. Xu et al., 2021).

Despite a general northward crustal thickening in the Himalaya-Tibet-Pamir and regional uniformity along the length of the Himalayas, geological and geophysical observations suggest along-strike tectonic variations as discussed below. In the east, the Tibetan plateau has thickened gradually due to the northward migration of the Indian plate (England & Houseman, 1985; England & McKenzie, 1982; C. Li et al., 2008; D. Shi et al., 2015). In contrast, the convergence was accommodated by large underthrusting in the west, forming the Western Syntaxis region that broadly covers the western Himalayas, the Kohistan-Ladakh arc, and the Pamir-Hindu Kush mountains (Burtman & Molnar, 1993; Kelly & Beaumont, 2021; Kufner et al., 2016). The Pamir-Hindu Kush region is characterized by deep seismicity to a depth of 300 km (Pegler & Das, 1998; Sippl et al., 2013) in contrast to Tibet, where earthquakes occur at less than 90 km (Liang et al., 2008; Schulte-Pelkum et al., 2019). Both the seismicity

pattern and seismic wave velocity images suggest complex northward subduction of the Indian plate beneath the Hindu Kush and the southward subduction of the Asian plate beneath the Pamir (Burtman & Molnar, 1993; W. Li et al., 2018). The dip of the Asian lithosphere flattens from the west to east of Tibet, whereas the Indian lithosphere seems to steepen (W. Li et al., 2018; J. Zhao et al., 2010, 2020). This also explains the difference in surface topography between western and eastern Tibet. Similar structural variation exists in the Himalayas in terms of the subduction geometry and age of granitoids (Dal Zilio et al., 2020; De Sigoyer et al., 2004; Eugster et al., 2018; Guillot et al., 2007; Leech et al., 2005).

The geophysical aspects of the India-Asia convergence zone have been largely dominated by seismological investigations from the central and eastern parts of the Tibet-Himalaya system (Klemperer, 2006; J. Li & Song, 2018; Nábělek et al., 2009; Nelson et al., 1996; Schulte-Pelkum et al., 2005; Shen et al., 2016; Yang et al., 2012; W. Zhao et al., 2011). These studies revealed evidence for the underthrusting of the Indian mantle lithosphere beneath Tibet (Kosarev et al., 1999), the underplating and subsequent eclogitization of the Indian lower crustal rocks beneath the Tibetan plateau (Nábělek et al., 2009; Sapin & Hirn, 1997; Schulte-Pelkum et al., 2005; F. Shi et al., 2018), and the partially molten and, viscous behavior of the middle crust of the Tibetan plateau (Caldwell et al., 2009; Hacker et al., 2014; Hetényi et al., 2011; Klemperer, 2006; Nelson et al., 1996; Yang et al., 2012). It is debated whether this weak middle crust beneath the plateau forms a pervasive channel flow (Beaumont et al., 2004; Burchfiel & Royden, 1985; Searle et al., 2011; Yang et al., 2012) or exists as disconnected and localized zones without a common source (Harrison, 2006; Hetényi et al., 2011). The continuity and applicability of these features to western Tibet and the Pamir and the role of the Karakoram Fault (KKF; Gilligan et al., 2015; Leech, 2008; Rai et al., 2006; Q. Xu et al., 2017) remain speculative due to the absence of experiments on a similar scale as in central and eastern Tibet. The situation improved in the last two decades with several broadband seismological experiments in western Tibet (L. Li, Murphy, & Gao, 2020; Razi et al., 2014; Wittlinger et al., 2004; Z. Zhang et al., 2014; J. Zhao et al., 2010), the Pamir-Hindu Kush (Kufner et al., 2016; Mechie et al., 2012; Schneider et al., 2019; Schurr et al., 2014), Kohistan-Ladakh-Kashmir (Mir et al., 2017; Rai et al., 2006), and the western Himalaya (Hazarika et al., 2017; Mahesh et al., 2013; Rai et al., 2006). In the section below, we discuss these experiments as well as the geology of the western Tibet-western Himalaya-Pamir-Hindu Kush region in general.

2. Geological Context and Crustal Structure

2.1. Geological Context

Continued convergence between India and Asia along the Indus Suture Zone (ISZ) formed the highest mountain systems, comprising the Himalayas, Tibet, and the Pamir-Hindu Kush. The Eurasian plate is an amalgamation of several crustal blocks. The prominent ones are: the Tien Shan and further north, considered as Precambrian to Paleozoic microcontinents; the Tarim and Tadjik rigid blocks south of the Tien Shan; and the Tibet-Pamir-Hindu Kush with Gondwana affinity. The southernmost part of Asia is an Andean-type margin with a 2,500 km long Trans-Himalayan (Kohistan-Ladakh-Gangdese) granitoid batholith. Subsequently, the deformation spread southward across Tibet, from the Tethys zone to the high Himalayan range and farther south. Major geological terrains, suture zones, and fault systems are shown in Figure 1. Burtman and Molnar (1993), Guillot et al. (2019), Kapp and DeCelles (2019), Royden et al. (2008), Sengör and Natal'In (1996), Yin (2006), and Yin and Harrison (2000) provide excellent reviews of the geological evolution of these terrains.

The Tibetan plateau is a collage of continental blocks that include, from north to south, the Songpan-Ganzi block, Qiangtang block (QB), and Lhasa block (LB), separated by the Jinsha Suture and Bangong-Nujiang Suture (BNS; Yin & Harrison, 2000). The BNS was formed in the Late Jurassic–Early Cretaceous when the Lhasa terrane collided with Asia's southern margin (Qiangtang terrane) to the north, followed by its northward subduction (Leier et al., 2007; Royden et al., 2008). The Tibetan plateau is joined to the Tarim Basin in the north by the Altyn Tagh Fault (ATF) and in the south to the Himalayas by the ISZ. Most of these Asian terranes are separated by narrow suture zones (Kapp & DeCelles, 2019; Yin & Harrison, 2000). The Tarim basin is underlain by stable Precambrian cratons (Zhu & Helmberger, 1998). The plateau's western limit corresponds to the traces of the ATF and KKF (Westaway, 1995).

The Pamir, at the northwestern margin of the India-Asia collision zone, is considered an along-strike continuation of Tibetan terranes (Burtman & Molnar, 1993; Schwab et al., 2004; Searle & Hacker, 2019), subject to a higher

degree of crustal shortening, metamorphism, and deeper exhumation, relative to the equivalent terrains in Tibet. Cenozoic gneiss domes, covering ~30% of the south Pamir (e.g., Shakhdara dome [SD]), central Pamir (e.g., Muskol and Shatput dome), and the east Pamir (Muztagh Ata dome) (see red shaded areas in Figure 1), expose the exhumed crust from ~30 to 50 km depth (Rutte et al., 2017; Searle & Hacker, 2019). The intermediate-depth (~70–300 km) seismicity in the Pamir outlines an arcuate slab dipping toward the east beneath the south-western Pamir and south beneath the eastern Pamir (Kufner et al., 2016, 2017; Mechie et al., 2012; Pegler & Das, 1998; Sippl et al., 2013). Beneath the Hindu Kush, the seismicity (~40–250 km depth) dips sub-vertically north-northwest (Kufner et al., 2016, 2017; Sippl et al., 2013).

To the south of the Pamir lie the Karakoram and Kohistan-Ladakh arc, separated by the Shyok Suture (or Main Karakoram Thrust, MKT). Kohistan-Ladakh is an intra-oceanic Cretaceous to Tertiary arc complex (Bard, 1983; Jagoutz & Kelemen, 2015; Tahirkheli, 1979) formed over a presumably north dipping subduction of the Tethys. The Kohistan-Ladakh arc has been thrust southward over the Indian crust along the Main Mantle Thrust (MMT)/ ISZ (Jagoutz & Kelemen, 2015; Tahirkheli, 1979). The southernmost geological unit of the study region is the Himalayan range, structurally dominated by various thrusts and detachments such as the Southern Tibetan Detachment (STD), Main Central Thrust (MCT), Main Boundary Thrust (MBT), and the Main Frontal Thrust (MFT). These thrust systems demarcate distinct Himalayan sequences from north to south, such as the Tethyan Himalaya (TH), Higher Himalaya (HH), Lesser Himalaya (LH), and Sub-Himalaya (Heim & Gansser, 1939; Yin, 2006). It is widely accepted that most of the thrust faults of the Himalayan range (MCT, MBT, and MFT) are rooted in a common decollement termed the Main Himalayan Thrust (MHT), which is a detachment between the base of the Himalayan thrust wedge and the top of the subducting Indian plate (Bilham et al., 2017; Seeber et al., 1981; Stevens & Avouac, 2015; Yin, 2006).

2.2. The Crustal Structure

During the last three decades, in addition to controlled source seismic experiments, several broadband seismological investigations have been performed to study the crust and mantle velocity structure of the Himalaya-Tibet region using earthquake waveform, ambient noise, and receiver function (RF; Acton et al., 2010; X. Bao et al., 2015; W. P. Chen et al., 2010; Galvé et al., 2006; Nábělek et al., 2009; Nelson et al., 1996; Owens & Zandt, 1997; Rai et al., 2006; Shen et al., 2016; Wittlinger et al., 2004; Yang et al., 2010, 2012; W. Zhao et al., 2011). These investigations show the progressive deepening of the Moho from 40 km in India to 50–60 km beneath the Himalayas, to 70 km beneath Ladakh, and ~90 km beneath the western Qiangtang-Kunlun. Earthquakes also accompany the unusually deep Moho beneath Kunlun to a depth of 90 km (Huang et al., 2011). Farther north, the Moho has been mapped at 44–60 km in the Tarim Basin and 55–60 km beneath the Tien Shan (Kao et al., 2001; Vinnik et al., 2004; Q. Xu et al., 2021; B. Zhang et al., 2020). The sedimentary cover in the Tarim Basin ranges from Proterozoic to Neogene age, with variable thickness from a maximum of up to 15 km in the depression center to 5 km in the central uplift area (Jia, 1997; Kao et al., 2001). Several seismological studies show varying northern extent and geometry of the underthrusting Indian lower crust to different latitudes in Tibet (L. Chen et al., 2017; L. Li, Murphy, & Gao, 2020; Nábělek et al., 2009; Wittlinger et al., 2004; Q. Xu et al., 2017; Z. Zhang et al., 2014; J. Zhao et al., 2010, 2020).

Seismic data from western Tibet reveal significant segmentation of the crustal structure beneath mapped tectonic boundaries (Z. Zhang et al., 2014), questioning the idea of the laterally flowing lower crust (Clark & Royden, 2000). This view is contradicted by Gilligan et al. (2015), who investigated the crustal structure of western Tibet (76–85°E), modeling RF and surface wave data jointly. In the middle-lower crust (20–40 km), shear wave velocity in Tibet is anomalously low and is interpreted to indicate the presence of partial melts (Makovsky & Klemperer, 1999; Owens & Zandt, 1997; Yang et al., 2012). The geometry of the partial melts of the Tibetan crust to the west of the Karakoram and the vertical extent of the KKF is a subject of debate (Caldwell et al., 2009; Leech, 2008; Searle et al., 2011).

Between 2008 and 2018, several seismological experiments were conducted to study earthquake patterns and the lithospheric structure of the Hindu Kush-Pamir region (Feld et al., 2015; Kufner et al., 2016; W. Li et al., 2018; Mechie et al., 2012; Schurr et al., 2014; Sippl et al., 2013). One of the significant findings of these studies is the ongoing subduction of the Eurasian continental lower crust, tracing the arcuate intermediate-depth seismic zone of the Pamir. However, the fate of the Indian lower crust in the Pamir remains speculative. These studies also reveal distinct low Vp (4.2–5.2 km/s) and high Vp/Vs ratio in the upper crust of the Tadjik Basin compared

to the high Vp and low Vp/Vs ratio in the Pamir, Tien Shan, and the Hindu Kush. W. Li et al. (2018) imaged a large-scale low-velocity anomaly in the crust at 20–50 km depth in the Pamir overlain by a high-velocity anomaly. The high-velocity zone collocates with the exposed gneiss domes, suggesting a linkage among the crustal deformation, partial melting, and exhumation.

In this study, we attempt to place constraints on the issues discussed above, namely the northern extent of the underthrusting Indian lower crust, the distribution of mid-crustal LVZs, and the depth extent of the KKF, using a combination of ambient noise and regional earthquake data sets, from which surface wave dispersion measurements were made following Bensen et al. (2007). We present a high-resolution 3-D shear wave velocity model, performed in two steps. First, we compute the Rayleigh wave group velocity maps for the region at a $0.5° \times 0.5°$ grid interval from period 5–60 s using earthquake and ambient noise data by Trans-dimensional Tree (TDT) Tomography (Hawkins & Sambridge, 2015). The dispersion data computed at grid nodes is then converted to shear wave velocity variation with depth by a Trans-dimensional, hierarchical Bayesian inversion (Bodin, Sambridge, Tkalčić, et al., 2012).

3. Data and Preliminary Analysis

3.1. Data

We use broadband seismological data from about 530 seismic stations operating between 1991 and 2016 (Figure 2a) during different time intervals. The seismic network includes stations from the PASSCAL experiments, the Global Seismograph Network, and various seismological experiments in Kyrgyzstan, Kazakhstan, Tajikistan, China, Nepal, and western Tibet. We also used data from the French deployments in western Kunlun and Kazakhstan and Indian deployments in the western Himalayas. Table S1 in Supporting Information S1 provides details of the network and stations used in the study. We analyzed the vertical component of the seismic records to extract the fundamental mode of Rayleigh wave dispersion using the ambient noise cross-correlation method and earthquake waveform analysis as discussed below.

3.2. Ambient Noise Analysis

Seismic ambient noise has been used to construct crust and mantle velocity structures with improved vertical and lateral resolution for almost two decades (e.g., Ritzwoller et al., 2011; Saha et al., 2020; Shapiro et al., 2005; Shen et al., 2016; Yang et al., 2010). The cross-correlation of ambient noise records between two stations is an estimate of Green's function (Shapiro & Campillo, 2004; Wapennar, 2004). We follow Bensen et al. (2007) and Schimmel et al. (2011) to process the ambient noise data. The pre-processing involves continuous waveform data from the vertical seismograph cut to 1-day length followed by removal of mean and trend, decimation to one sample per second, correction for instrument response, and bandpass filtering from 0.01 to 0.25 Hz range (4–100 s period range). Next, we compute inter-station Green's functions from ambient noise time series using the phase cross-correlations (PCCs) technique (Schimmel, 1999; Schimmel et al., 2011). Based on analytic theory, the PCC technique uses phase coherence to find similarities between two signals as a function of lag time without the need for explicit pre-processing (i.e., temporal normalization and spectral whitening). The resultant output of the PCC is unbiased amplitude (see Text S1 in Supporting Information S1) and is widely used to detect weak coherent signals (e.g., Acevedo et al., 2021; Hable et al., 2019; Ventosa et al., 2019). Finally, the daily cross-correlations are stacked by the time-frequency phase weighted stack (tf-PWS) approach (Schimmel & Gallart, 2007; Schimmel et al., 2011). Here, each linear stack is weighted by a coherency measure of its instantaneous phase to improve the signal-to-noise ratio (SNR). We separate negative (acausal) and positive (causal) components and stack them to obtain symmetric cross-correlations (Figure 2b).

The final stacked cross-correlations are used to compute group velocity dispersion using the Frequency-Time-Analysis (FTAN) method (Levshin & Ritzwoller, 2001). The FTAN method uses an analytic signal from a waveform filtered at a central period to obtain an instantaneous amplitude, which provides group velocity corresponding to the maximum amplitude. The uncertainty in group velocity measurement is computed by generating 20 different combinations of 75% of daily cross-correlations selected randomly to obtain 20 stacks through bootstrapping and estimating their standard deviations (e.g., Acevedo et al., 2019). We retain dispersion data that has an interstation distance $\geq 3\lambda$ (λ is wavelength), and has at least 10 random stacks with SNR ≥ 10. For a typical station pair GARM-GUGE, the group velocity dispersion computed from the bootstrapping and the corresponding SNR are

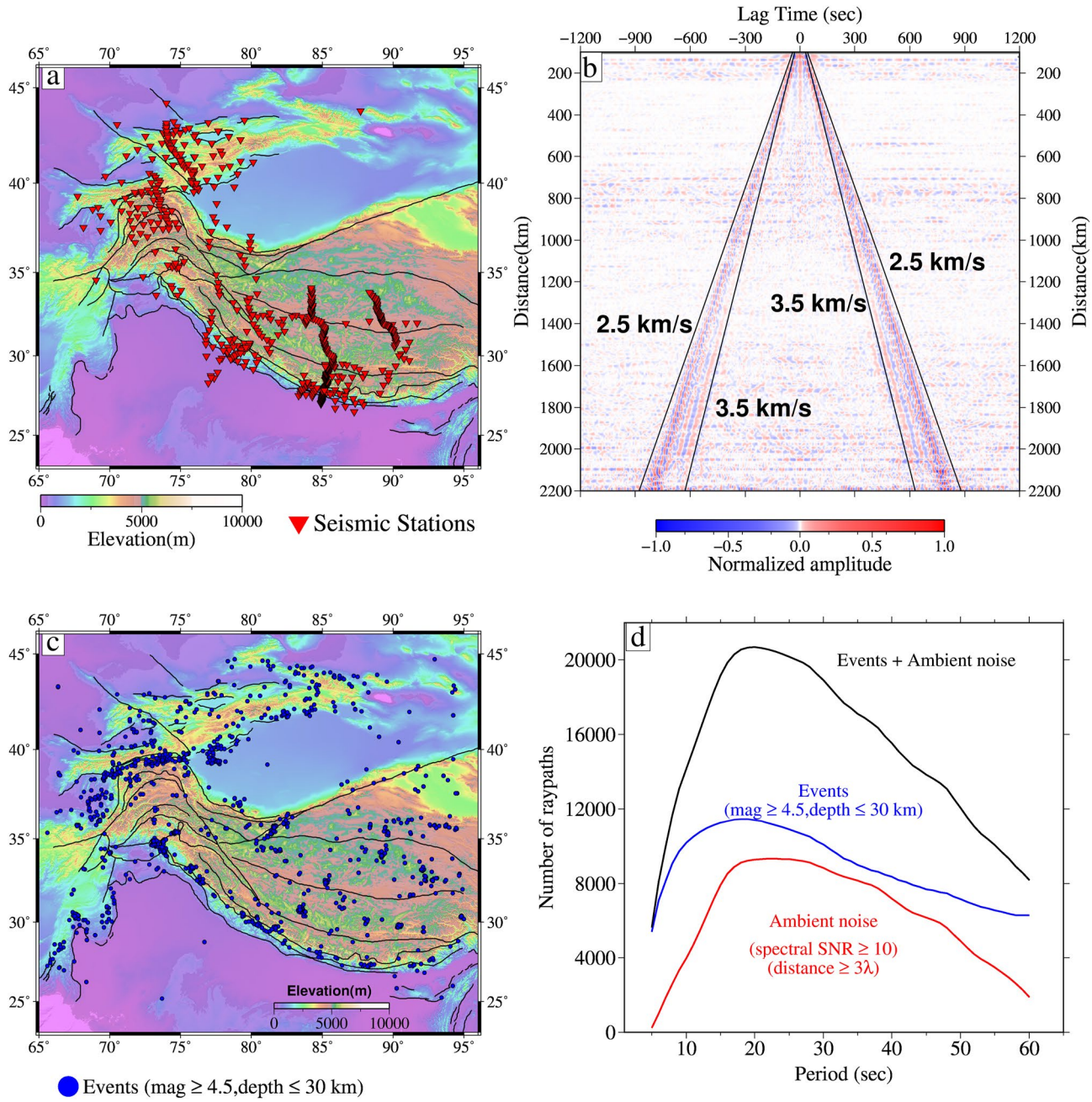

Figure 2. Ambient noise and event data. (a) Locations of seismic stations (red inverted triangles). (b) Symmetric stacked cross-correlations plotted with increasing interstation distance. Black lines indicate signal window of the estimated Green's function with velocity from 2.5 to 3.5 km/s. (c) Location of earthquakes marked as blue dots (mag ≥4.5, depth ≤30 km) used for dispersion measurement. (d) Number of dispersion measurements using ambient noise (red line), earthquake waveforms (blue line) and combination of both (black line) at different periods.

presented in Figures S1a–S1c in Supporting Information S1. To validate the group velocity measurement from ambient noise, we also compared it with the group velocity dispersion computed from an earthquake of magnitude five in the proximity of GARM recorded at GUGE (Figure S1d in Supporting Information S1). Both the dispersion curves are largely consistent with each other, although there are mismatches at 20–30 s, and 45–60 s. This difference, which is around 2% of the event dispersion, probably indicates inadequate source parametrization of the event, low SNR of the event and/or noise dispersion, and inhomogeneity of the ambient noise wavefield (see F. Bao et al. [2014] for a detailed discussion). After applying the selection criteria mentioned earlier, we are

left with 9,794 (out of 22,958 initial) inter-station dispersion measurements with Rayleigh wave group velocity data from period 5–60 s for further analysis.

3.3. Earthquake Data Analysis

To improve the raypath coverage, we also used dispersion measurements from local and regional earthquakes located within our study region. Around 1,261 earthquakes with a magnitude greater than 4.5 and a depth of less than 30 km were selected from the reviewed ISC catalog between 1991 and 2016 (Figure 2c). Like the ambient noise analysis, dispersion measurements were made using the FTAN method, resulting in additional dispersion data along 12,932 raypaths. Thus, the combined noise and earthquake raypaths of 22,726 provide dispersion measurements for the period range of 5–60 s. Figure 2d provides details of the number of raypaths derived from ambient noise and earthquake data at different periods.

4. Group Velocity Tomography

The inter-station Rayleigh wave group velocities obtained from the ambient noise and earthquake data are used to generate 2-D group velocity maps at each time period in two stages. First, the initial inversion for analyzing data quality and generating group velocity maps, followed by the Bayesian Trans-dimensional inversion. For the initial inversion, we performed a number of linearized subspace inversions with the Fast Marching Method (FMM; Rawlinson & Sambridge, 2005) for a series of synthetic discrete spike tests (checkerboard patterns with spacing between oscillatory positive and negative anomalies) to investigate the resolving power of the data set. Following Rawlinson and Spakman (2016), we used three different-sized ($1° \times 1°$, $0.5° \times 0.5°$, and $0.3° \times 0.3°$) positive and negative anomalies with 10% perturbation from 3 km/s separated by 1° spacing. The results of the sensitivity tests at five representative periods (5, 10, 20, 40, and 60 s) are presented in Figure S2 in Supporting Information S1. The recovered checkerboard patterns corresponding to $1° \times 1°$ and $0.5° \times 0.5°$ input models show excellent recovery of negative and positive anomalies at all periods without lateral smearing within the study region. Model recovery for a $0.3° \times 0.3°$ input model shows small-scale lateral smearing near the Peshawar Basin, Hindu Kush, Tadjik Basin, and Tarim Basin. The major part of the study region that includes the Pamir, Kohistan-Ladakh, western Tibet, and a large part of the central and western Himalayas is well resolved. Further decrease in block size degrades the velocity image, and therefore, we preferred a $0.5° \times 0.5°$ block dimension as the optimal lateral resolution for this study. We then performed the subspace inversion from period 5–60 s to obtain reasonable starting models. At this stage, we used the subspace solution models as an outlier removal tool. There are many ways to remove low-quality data points. For example, one can use thresholds on the level of error in the source location or azimuthal coverage given by event catalogs. In this study, we used an approach based on the coherency between observed travel-times. For a period, we remove all travel-time data points with residuals more than two standard deviations (Figure S3 in Supporting Information S1) before performing Bayesian tomography.

In stage 2, we employed the Bayesian TDT tomography with wavelet parametrization (Hawkins & Sambridge, 2015), using the final subspace models as the starting models. Although the TDT approach does not depend on the choice of the starting model (e.g., Rosalia et al., 2020), the use of reasonable starting models in Bayesian tomography helps in the early convergence of model parameters and significantly reduces computational time. The TDT scheme has flexibility in terms of model parametrization using wavelet tree structures, estimation of data noise level, which affects model complexity, and robust computation of model uncertainty, resulting in a data-driven or parsimonious final model. The method has been successfully applied in several geophysical studies (e.g., Hawkins et al., 2018; Pilia et al., 2020; Rosalia et al., 2020). We briefly discuss the TDT approach in the following section. For a detailed description, we refer to Hawkins and Sambridge (2015).

4.1. Bayesian Trans-Dimensional Tree Tomography

The TDT tomography scheme (Hawkins & Sambridge, 2015) uses a multi-resolution wavelet tree structure to represent a velocity field with a single-pixel mean (at the root of the tree) and a hierarchy of local deviations (i.e., wavelet coefficients) from coarse to fine-scale. The method predicts group travel-time using the FMM and subsequently adopts a Bayesian inversion using a reversible-jump Markov chain Monte Carlo algorithm (rj-McMC; Green, 1995) to construct an ensemble of solution models. These solution models collectively define a posteriori

probability distribution $p(\theta|d)$ which gives the probability of model parameters θ given observed data d using the Bayes theorem (Bayes, 1763):

$$p(\theta|d) \propto p(d|\theta) \times p(\theta), \tag{1}$$

where $p(\theta)$ is prior probability distribution or a priori, which is a probability on the plausible range of model parameters, before observing the data. $p(d|\theta)$, known as the likelihood, represents the probability of observing d, given a set of model parameters. Assuming data errors are distributed as a Gaussian distribution, the likelihood writes:

$$p(d|\theta) = \frac{1}{\sqrt{(2\pi)^n |C_e|}} \exp\left\{ -\frac{(G(\theta) - d)^T C_e^{-1} (G(\theta) - d)}{2} \right\}, \tag{2}$$

where the operator G represents data predictions from the model θ and, C_e is the data error covariance matrix ($C_e = \sigma_d^2 I$, where σ_d is the standard deviation of data noise). The level of σ_d controls how well the predicted data should fit the actual observations, which further affects the complexity of the recovered models. For example, in the case of large data errors, a smooth and simple model will be enough to explain the observations. Quantification of the data noise before the tomographic inversion is difficult, so a hierarchical Bayesian framework is often used (Bodin, Sambridge, Rawlinson, & Arroucau, 2012; Malinverno & Briggs, 2004), where the data noise is treated as an unknown parameter to be inverted for. In the TDT approach, a scaling term (λ, also called the hierarchical error scale) is used to scale the standard deviation of data noise (σ_d) to get an estimate of true data noise, $\sigma_t = \lambda\sigma_d$, where λ is an unknown to be inverted for.

In the trans-dimensional framework (or rj-MCMC), the parametrization of the model (θ) and its size can change during inversion steps using the Birth/Death scheme (Geyer & Møller, 1994; Green, 1995). The key advantage of the trans-dimensional steps combined with the hierarchical error estimation is that the data constrain the information present in recovered models without explicit regularization. The rj-McMC sampler using an iterative approach generates a candidate model (θ') from a current model (θ) using a proposed distribution, $q(\theta'|\theta)$. The new candidate model (θ') is accepted or rejected based on generalized Metropolis-Hasting-Green (Green, 1995) acceptance criteria:

$$\alpha\left(\theta', \theta\right) = \min\left\{ 1, \frac{p(\theta')}{p(\theta)} \frac{p(d|\theta')}{p(d|\theta)} \frac{q(\theta|\theta')}{q(\theta'|\theta)} |J| \right\}, \tag{3}$$

where $|J|$ is the Jacobian determinant that maintains detailed balance when the model dimension changes.

The prior $p(\theta)$, in this case, is the probability of available information about the plausible range of group velocity values. The prior mean (or the reference group velocity) is given by the average of the inter-station group velocity measurements. Since the TDT approach uses wavelet tree structures to represent the velocity field, the prior group velocity is provided in terms of wavelet coefficients. We used a Laplacian prior for the wavelet coefficients. The width of the Laplacian prior was chosen following Hawkins et al. (2018). We performed a number of tests with different prior widths and sampled the prior to examine the resultant "a priori" distribution for group velocities. With the increasing width of the Laplacian prior, the range of group velocity values expands (Figure S4 in Supporting Information S1). We selected the width of the Laplacian prior on wavelet coefficients such that, for a mean group velocity of 3 km/s, the prior group velocity ranges from 2.4 to 3.6 km/s. It is important to note that the "a priori" on the group velocity indicates the breadth of the model space (i.e., group velocity values) that is sampled during the inversion and is independent of the data set used; thus, it provides no information about the uncertainties associated with the data.

Independent Markov chains are assumed to converge when the negative log-likelihood reaches an equilibrium state. To speed up the Markov chain convergence, we used group velocity maps obtained from the subspace FMM inversion as the starting model, as discussed earlier. We ran a total of 24 parallel Markov chains, each with 1.5 million samples. The first one million samples were discarded as burn-in steps, and every 100th sample of the remaining 500,000 samples was visited to obtain the final ensemble models. The level of knowledge about the group velocity values is provided by these ensemble models, which form the posteriori probability distribution $p(\theta|d)$ discussed earlier. To visualize this probabilistic solution, different projections can be used for interpretation: the mean, maximum a posteriori (MAP), median, standard deviation, credible intervals, etc. Here in this

study, we use the mean and standard deviation of the final ensemble models to derive group velocity maps and associated uncertainty, respectively. We acknowledge that in a Bayesian inversion, the choice of the prior distribution does affect the form of the posterior distribution. To investigate this effect, we generated a set of group velocity maps with larger prior widths at the 40 s period (Figure S5 in Supporting Information S1). The group velocity maps obtained with different priors show broad consistency in the recovered structures.

Figure S6 in Supporting Information S1 depicts the convergence of various parameters at the 40 s period (e.g., number of coefficients, negative log-likelihood, and hierarchical error scale) with 1.5 million iterations. The number of wavelet coefficients (i.e., the number of model parameters required by the data) converges to about 500, which is much less than what would be required for an image with 64 × 64 pixels (i.e., 0.5° × 0.5° grid nodes in this study). Similarly, the hierarchical error scale (λ) approaches a value of between 0.9 and 0.85, suggesting that the initial data noise was slightly overestimated. Additionally, the negative log-likelihood reaches equilibrium in the early stages of iterations due to the robust initial model. A test inversion with more Marko chains/number of iterations shows no change in output models (Figure S7 in Supporting Information S1), further suggesting the early convergence. To ensure that the two independent data sets, that is, ambient noise and earthquake, produce consistent velocity images, we generated three group velocity maps at 40 s using ambient noise data only, earthquake data only, and the combination of both (Figure S8 in Supporting Information S1). While the velocity images are similar, combining the two data sets increases the total raypaths, thereby providing improved resolution.

4.2. Lateral Variations in Rayleigh Wave Group Velocity

Following the above approach, group velocity maps are constructed from time periods of 5–60 s at 1 s intervals on a 0.5° × 0.5° grid interval (Figures 3a–3g, see Figure S9 in Supporting Information S1 for full grid tomographic maps). The general consistency of structural features is observed across all periods. The relationship between the group velocity at a period and the corresponding depth of investigation is shown by the sensitivity kernel (Figure 3h). The group velocity at 10−15 s with a peak sensitivity at ∼8–10 km below the Earth's surface represents the upper crust, sedimentary basins, and fold belts (Pasyanos, 2005). At the shorter periods (10–20 s), the sedimentary basins (Tarim, Tadjik, Ferghana) and the Himalayan arc are characterized by low group velocities due to 5–15 km thick sediments, whereas the interiors of both the Pamir and Tibet have higher group velocities. For a longer period (30−40 s) with peak sensitivity at 30–45 km depth, the sedimentary basins and the Himalayan arc have higher group velocities. In contrast, the Pamir and Tibet have lower group velocities at 40–60 s period (with peak sensitivity depth ∼ 50–80 km), possibly due to large crustal thickness (up to 90 km) and widely reported low mid/lower crustal shear velocity of ∼3.3 km/s. The low velocity in the Pamir and western Tibet is dissected by a high-velocity N-S linear feature at roughly 76°E. The high-velocity anomaly is largest in the Kashmir-Zanskar Himalaya and lowest in Ladakh and the neighboring areas. The robustness of this feature is supported by a number of least-squared tomographic inversions with various regularization parameters shown in Figure S10 of Supporting Information S1.

The uncertainties in group velocities, ray hit counts, and the travel-time residuals are presented in Figures S11–S13 of Supporting Information S1. The large standard deviations associated with the group velocity maps correspond to the areas with a lack of raypath coverage, such as the northern Indian Peninsula and, the north-eastern Tarim Basin. At longer periods (≥40 s), the central Himalaya, southern Tibet (east of 81°E), and some parts of the western Himalaya south of the Ladakh arc show relatively higher uncertainties. Our group velocity maps provide significant improvement due to better raypath coverage and lateral resolution compared with previous experiments in the study region (e.g., Gilligan & Priestley, 2018; Khan et al., 2017; Kumar et al., 2019; Shen et al., 2016; Yang et al., 2012). Since group velocity at a given period is an integrated effect of velocity over a range of depths, we invert the dispersion curve at a given geographical location to constrain a 1-D model of shear wave velocity.

5. 1-D Velocity-Depth Models

Group velocities at each of the grid-points in 2-D tomography maps are used to derive shear wave velocity (Vs) variation with depth using a 1-D inversion scheme based on a hierarchical, trans-dimensional Bayesian inversion (Bodin, Sambridge, Tkalčić, et al., 2012). We then interpolate the 1-D shear velocity model obtained at each

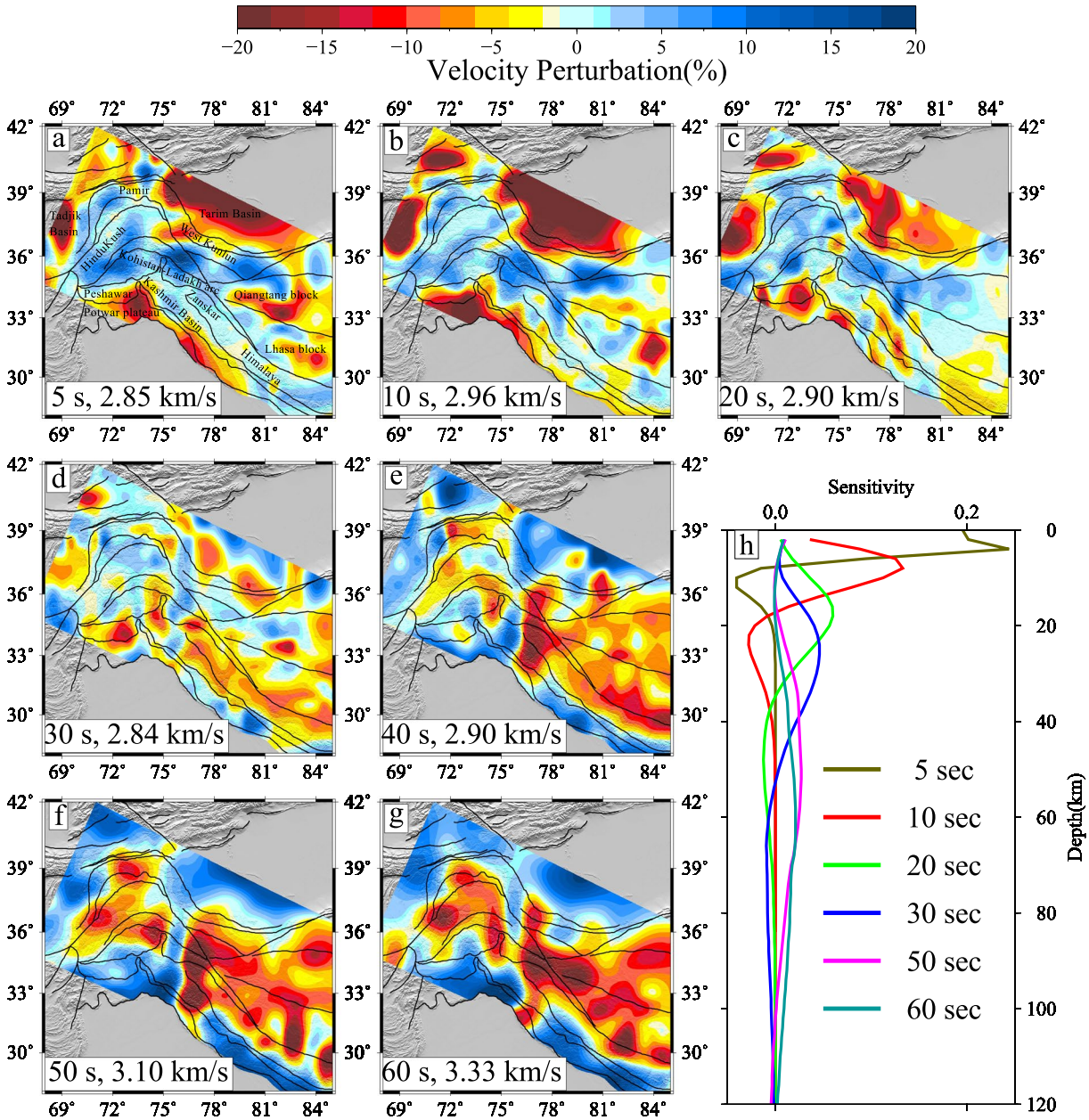

Figure 3. Rayleigh wave group velocity maps. (a–g) Group velocity maps from period 5–60 s plotted as percentage deviations from the regional mean (marked at the bottom of each map). (h) Sensitivity kernels for Rayleigh wave group velocities at periods 5–60 s. The corresponding standard deviations, raypath density, and group delay time are presented in Figures S11−S13 in Supporting Information S1.

grid point to produce a 3-D shear wave velocity model. The basic framework of the Bayesian inversion with the trans-dimensional sampling is the same as discussed in Section 4.1. The model parametrization is made dynamic by considering the number of layers, position, and shear velocity as unknowns during the inversion. Like the 2-D group velocity inversion, we consider the data noise level (σ_d) as an unknown parameter to be inverted here (although the standard deviations obtained from the 2-D inversion could also be used as the data noise). We use broad uniform priors on various parameters, such as the number of layers, data noise level, and shear wave velocities. The lower and upper bounds of the prior on shear wave velocity are defined as $m_0(1 \pm w)$, where m_0 is a reference model (or mean of the prior on shear velocities), and w is the width of perturbation. We use the subroutine DISPERSE80 (Saito, 1988) for the forward calculation of the group velocities given a 1-D model.

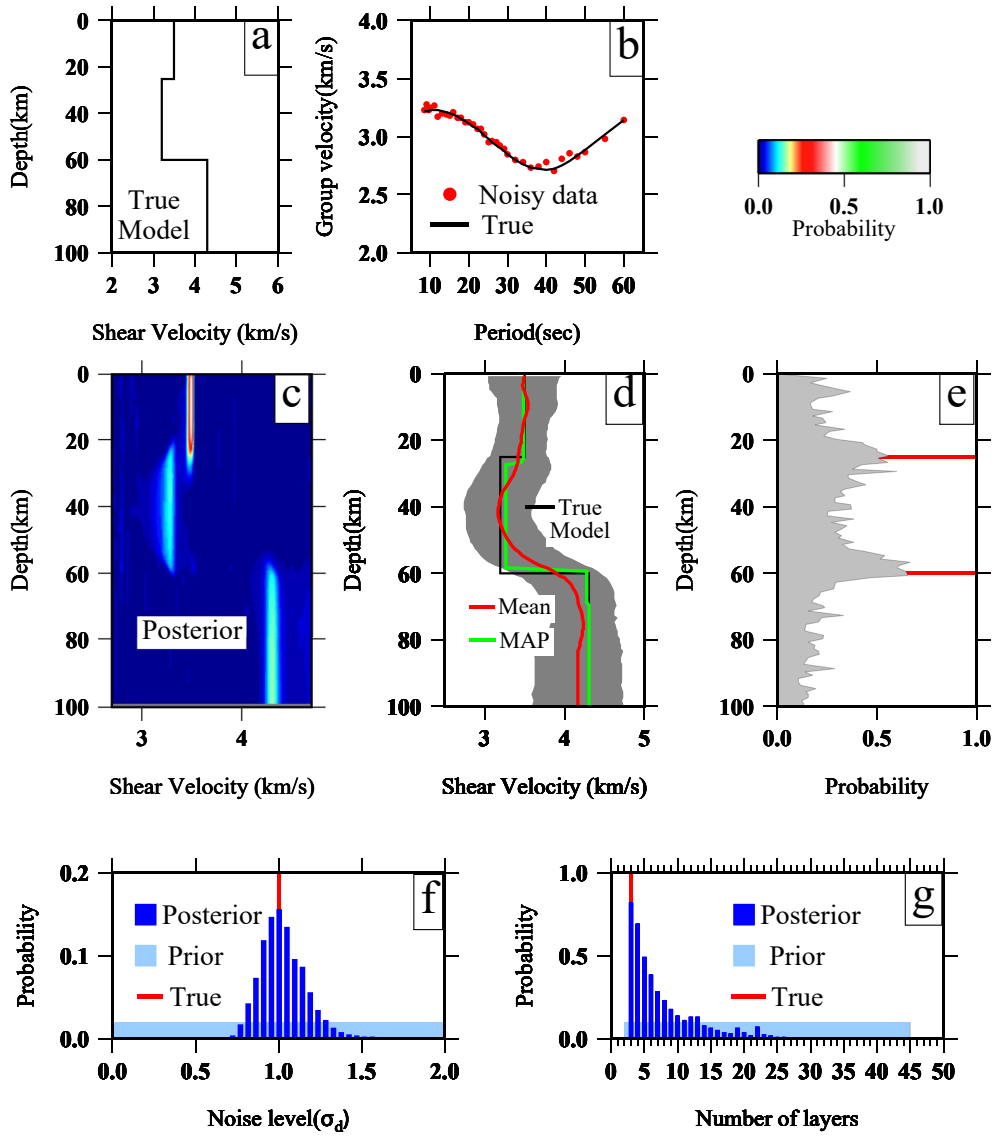

Figure 4. Demonstration of Trans-dimensional hierarchical inversion. (a) An example 3 layered shear velocity model (black line). (b) Synthetic dispersion data (with added noise). (c) Posterior probability after inversion shown in color data. (d) Output velocity model in terms of posterior mean (red) and maximum a posteriori (MAP) (green) compared with the true model (black). The gray shaded area represents one standard deviation bounds. Posterior probability on position of discontinuities as a function of depth (e), data noise level (f) and number of layers (g) are shown with the red line indicating true values. A half-space model with shear wave velocity at 4 km/s was used as the reference model.

To illustrate the inversion methodology, we performed a synthetic test using a 3-layer earth model (Figure 4a). Synthetic group velocities from 5 to 60 s were computed, and random Gaussian noise (1% of the synthetic value) was added (Figure 4b). We used uniform prior bounds on the number of layers (2–45) and data noise level (0–2). The inversion was performed with a half-space reference velocity model (m_0) with a maximum allowed perturbation of 40% (i.e., $w = 0.40$). Computed mean and MAP from the resultant posterior distribution are compared to the input model (Figures 4c and 4d), showing that both amplitudes and patterns are well resolved. The posterior distribution on the location of discontinuities, level of data noise, and number of layers (Figures 4e–4g) also peak at actual values.

We performed two additional synthetic tests (details in supplementary document, Texts S2 and S3 in Supporting Information S1, Figures S14 and S15 in Supporting Information S1) to analyze the effect of the prior distribution on inverted models and the resolution of the LVZ in the crust. Using three different reference models (m_0), we

demonstrate that the choice of the reference model does not influence the mean of the posterior (Figure S14 in Supporting Information S1), and the crustal structures can be reliably recovered within the period range considered in this study. We experimented with synthetic models having LVZs of varying thicknesses and amplitudes in the depth range of 30–50 km (Figure S15 in Supporting Information S1). The inversion results show that our data can reliably resolve an LVZ with a minimum thickness of 5 km.

After various synthetic tests investigating the resolving power of the dispersion data in crustal imaging, we performed the final 1-D inversion using 480 parallel Markov chains with a maximum iteration of 100,000. The first 50,000 samples were discarded as "burn-in" samples, and every 10th sample of the remaining 50,000 samples constitutes the final ensemble of solution models. The mean and standard deviations of the final ensemble model were used as the average shear velocity and associated uncertainty, respectively. For the reference velocity model (m_0), we used a smoothly layered average model of Tibet obtained from averaging the 1-D models of Shen et al. (2016). We set uniform priors on the number of layers (2–100) and the data noise level (0%–10%) by allowing the shear wave velocity to perturb up to 40% from the reference model within a maximum depth of 100 km. A 3-D shear velocity with $0.5° \times 0.5°$ grid intervals was constructed by interpolating velocity-depth models at grid points. To strengthen the reliability of the inversion result, we compared our velocity model with previous studies at different locations such as ISZ, Western Syntaxis, and Hindu Kush (Figure S16 in Supporting Information S1). Also, we generated a velocity depth section along the profile of Gilligan et al. (2015) in the western Himalaya and contiguous Tibet. We observe a general similarity between the present work and earlier velocity models, albeit with local variations due to different data, methodology, and spatial resolution.

6. The Shear Wave Velocity Structure and Regional Variability

6.1. The Shear Wave Velocity Model

We discuss general features of the computed shear velocity model over the study region. Figure 5 shows maps of shear wave velocities at depths of 10, 30, 50, and 70 km relative to the regional average. At shallower depths (~10 km), parts of the Tarim, Tadjik, and Ferghana sedimentary basins show prominent low velocities due to thick sediments. Furthermore, the Himalayan arc has low velocities in its western and northwestern segments (west of 78°E), indicating the Sub Himalayan sedimentary sequence that is wider in the western Himalaya than in the central Himalaya (DiPietro & Pogue, 2004; Yin, 2006). However, the interior of the Pamir, Hindu Kush, and west Tibet mostly contains high shear wave velocities.

At 30 km depth, we observe LVZs across western Tibet, Ladakh-Karakoram, and the Pamir. The lowest velocities are present near the Ladakh-Karakoram-Nanga Parbat zone. We have marked four prominent LVZs corresponding to western Tibet (L4), the Zanskar Himalaya-Ladakh-Karakoram (L3), the south-western Pamir-Hindu Kush (L1), and the north-northeastern Pamir (L2) by blue dashed polygons in Figure 5b. Low velocities in western Tibet (L4) are well documented, and are possibly due to partial melts or aqueous fluid (Gilligan et al., 2015; Yang et al., 2012). Beneath Ladakh and Karakoram, the LVZs (L3) indicate the presence of young granites (Searle et al., 2010). In the Zanskar Himalaya, the LVZs collocate with large-scale migmatites and granites. Low velocities from eastern Kohistan through Ladakh continue to southern Tibet. Beneath the Pamir-Hindu Kush, the LVZs (L1, L2) largely correlate with the surface exposure of gneiss domes (marked as red polygons in Figure 5b) formed due to melting at a depth of 30–50 km and transported upward (Searle & Hacker, 2019). For example, the SD correlates with the LVZs (L1) in the southwestern Pamir, which appear to be continuous with the Hindu Kush and Tadjik Basin, and the Muztagh Ata dome (MA) correlates with the LVZs (L2) in the northeastern Pamir.

The LVZs become more widespread at 50 km depth (Figure 5c). Its continuity can be observed from western Tibet to the Pamir-Hindu Kush region through Ladakh and Karakoram. The crustal LVZs progressively deepen northward, starting from ~20 km in the western Himalaya to ~30 km in the Indus suture zone, southwestern Tibet, Karakoram, Hindu Kush, and the southern Pamir. Farther north, we observe LVZs in northwestern Tibet, the central and south Pamir, and the northern Hindu Kush at depths of ~40–50 km. At a deeper depth of 70 km, most parts of the Himalaya and Ladakh are characterized by higher velocities, representing the uppermost mantle. In contrast, western Tibet-Kunlun and the Pamir-Hindu Kush regions have lower velocities (correlating with deep seismicity), possibly due to the thicker crust and higher mantle temperature (Rai et al., 2006; Schneider et al., 2019; Z. Zhang et al., 2014). An interesting feature of the velocity map is a high-velocity anomaly in the Kashmir Himalaya appearing at greater depths (e.g., at 50 and 70 km depth in Figure 5), that probably extends

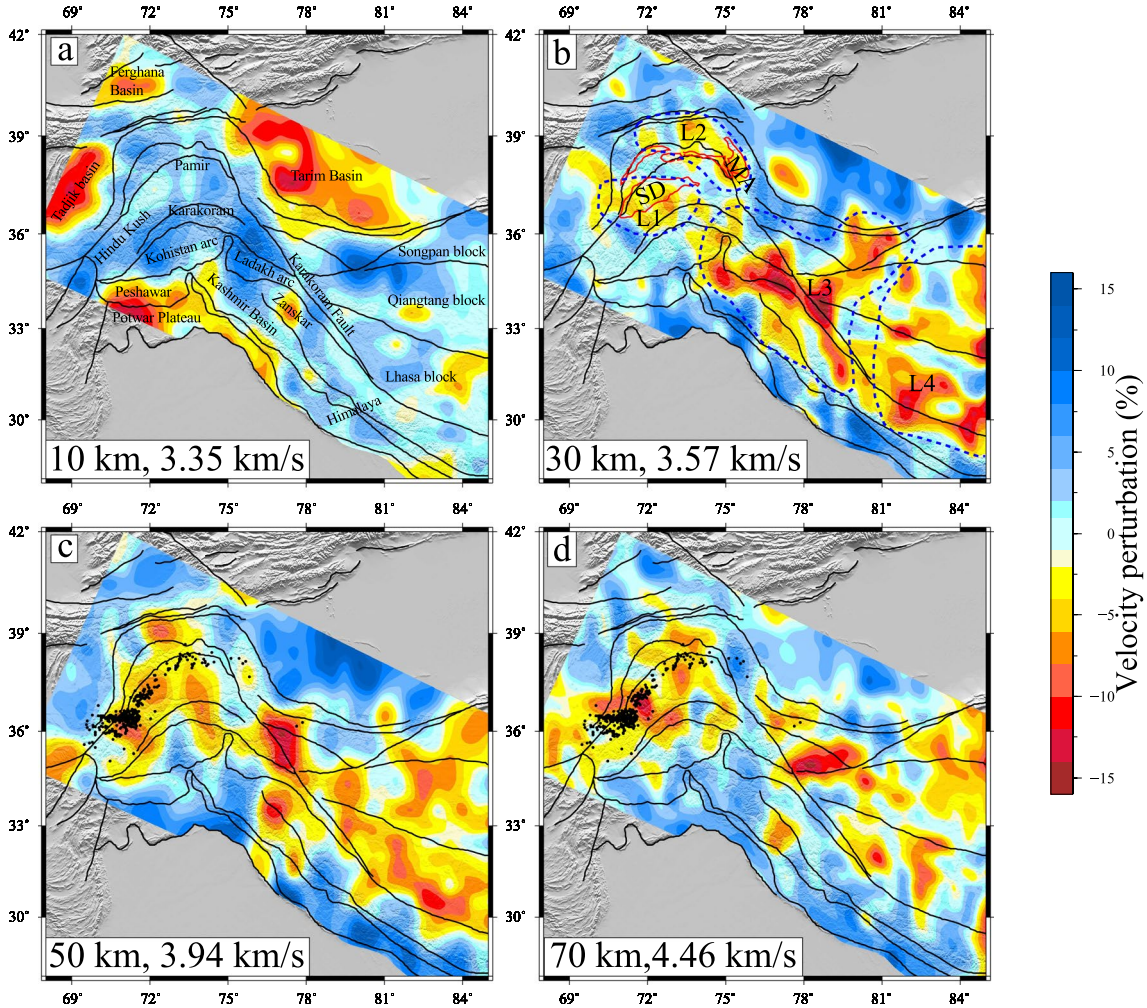

Figure 5. Shear wave velocity maps at depths of (a) 10, (b) 30, (c) 50, and (d) 70 km plotted as perturbations from the regional mean velocity (marked at the bottom of each map). The mean velocity is calculated by the area average of 3-D velocity model at different depths. The black dots in (c and d) represent deep seismicity (>50 km). The solid red polygons in (b) show gneiss domes of Pamir, and the dashed blue polygons marked as L1, L2, L3, and L4 are the low-velocity zones at 30 km depth. SD, Shakhdara dome; MA, Muztagh Ata dome.

further north as shown in group velocity maps (Period ≥40 s in Figure 3 and Figure S10 in Supporting Information S1), adjacent to an LVZ extending from the Zanskar Himalaya in the south to Ladakh-Karakoram and up to the western Kunlun (76–78°E). Three NW-SE velocity-depth profiles (Figure S17 in Supporting Information S1) show that the high-velocity anomaly (at 75–76°E) is most prominent in the Kashmir-Zanskar Himalaya (depth >30 km and Vs > 3.8 km/s) and weakens further north. It is noteworthy that the southern extension of this anomaly matches with a significant structural boundary in the Ganga basin (at 75°E) that segments the Indian lithosphere (Saha et al., 2020). Detailed exploration of this feature and its implications in the context of India-Asia convergence is a subject of future study.

The uncertainties associated with the velocity model can be analyzed in terms of the posterior standard deviations presented in Figure S18 in Supporting Information S1. There is a continuous increase in uncertainties with depth. The relatively large uncertainties at greater depths possibly indicate the combined effect of the trade-off between the crust and upper mantle velocities and the poor sensitivity of our data to structures below 80 km. Note that surface waves are sensitive to the spatial average of velocities over a longer wavelength, and the solution to the inverse problem is highly non-unique. This is represented by the wider posterior distributions (or large standard deviations) given broad priors and flexible model parametrizations used in this study (see Text S4 and Figure S19 in Supporting Information S1). Additionally, a synthetic test considering different Moho depths and mantle velocities shows that the crust-mantle velocity trade-off has minimal effect on the recovered crustal

structures (Figure S20 in Supporting Information S1), thereby enhancing the reliability of the crustal velocity model presented here.

6.2. The Crustal Structure and Regional Variability

To investigate the detailed crustal structure and its correlation with surface geology and possible earth processes, we present the velocity structure along six south-north profiles from the Himalayas in the south to the Pamir/Tarim in the north (Figures 6 and 7).

The continental crust is often divided into the upper, middle, and lower crust with a characteristic shear wave velocity Vs < 3.6, 3.6–3.8, and, >3.8 km/s, respectively. The shear wave velocities in the lower crust higher than 4.0 km/s above the Moho are due to rocks of mafic composition (garnet granulite) and are widely referred to as the 7x layer (Vp > 7 km/s; Christensen & Mooney, 1995; Rudnick & Fountain, 1995). This high-velocity lower crust (HVLC), can be formed by various mechanisms, such as magmatic additions to the crust in the form of mafic magma or through magmatic differentiation processes, or by the mechanical addition of high-velocity materials to a crustal column during collisional or accretionary tectonic events (Schulte-Pelkum et al., 2017). Such a high-velocity layer (Vs > 4 km/s) in the lower crust may also represent an eclogite that is reportedly widespread in the Himalayan collision zone (Nábělek et al., 2009; Sapin & Hirn, 1997; Schulte-Pelkum et al., 2005). Earlier proposed crustal doubling in Tibet and the Himalayas by underthrusting of the Proterozoic northern margin of the Indian plate requires the presence of a mafic layer with high seismic *P* wave velocity (Vp > 7.0 km/s) above the Moho (Sapin & Hirn, 1997; Schulte-Pelkum et al., 2005). This is consistent with the velocity structure of the Indian crust to the south of the Ganges basin that suggests a gradational Moho with the lower crust Vs ∼4.1–4.3 km/s, a Moho depth of 45–50 km, and the uppermost mantle velocity of 4.55 km/s obtained from joint inversion of RF and surface wave dispersion data (Julia et al., 2009). Such a Moho shear velocity is predicted by thermodynamical modeling corresponding to a crust with the composition proposed by Rudnick and Gao (2003) with a low thermal gradient of ∼10 K/km (Diaferia & Cammarano, 2017). Existing seismological data suggest the HVLC and high-velocity upper mantle in the Himalayas and southern Tibet correlating with the presence of seismically fast lower Indian cratonic crust and lithosphere beneath southern Tibet (Nábělek et al., 2009; Sapin & Hirn, 1997; Schulte-Pelkum et al., 2005). The northern termination of the HVLC may represent the end of the Indian lower crust (DeCelles et al., 2002). With an increasing thermal gradient, the Moho velocity is reduced to around 4.2 km/s. The role of increasing thermal gradient on shear velocity needs to be considered carefully while using it as a proxy for mapping the Moho depth.

We did not compute the Moho depth due to a trade-off between the Moho depth and the crust-mantle velocity structure in the inversion of surface data (Lebedev et al., 2013) and also due to poor resolution of the velocity model beyond 80 km as a consequence of the limit on the available longer period surface wave data. Instead, we marked the Moho depth on the velocity section obtained from earlier studies primarily using RF/and or its joint inversion with surface wave data (top right panel in Figure 6). Also, we used a broad constraint on the Moho depth based on Sn velocity tomography result that suggests an average value of 4.55 km/s for the Himalaya-Tibet, which reduces by 3%–4% over northern Tibet (Pei et al., 2011). The gradational nature of the crust observed south of the Ganga basin continues beneath the Himalayas and western Tibet (Gilligan et al., 2015). A gradational Moho cautions against the use of the H-κ stacking technique in this region. However, if along with PS conversion, one of the Moho multiples is also clearly observed, the Moho depth could be properly mapped. To be consistent in this study, we used the Moho depth, preferably from studies using joint inversion of RF and surface wave dispersion data, except at a few locations where the Moho depth from common conversion points (CCP) depth migration is used. The depth migration in the CCP involves a velocity-depth trade-off in RFs and may result in an error in the Moho depth mapping in the absence of a reliable migration velocity. The Moho depth could be more accurately mapped by creating self-consistent images using PS conversion and the Moho multiples. Gilligan et al. (2015) provide a detailed analysis and comparison of Moho depth computed using joint inversion and CCP migration in western Tibet. Caldwell et al. (2013) and He et al. (2018) evaluate the effects of different velocity models on migration results and demonstrate that different velocity models with a fixed Vp/Vs ratio of 1.75 lead to up to a ∼2.5 km Moho variation for a crustal thickness of 80 km. Nevertheless, assuming the ∼2% variation in each parameter, Vp (or Vs) and Vp/Vs ratio, about up to a ∼5% variation in the Moho depth is shown. A detailed analysis by Shen et al. (2016) shows a variation of about 4 km in picking Moho depth beneath Tibet for inversion of surface wave data.

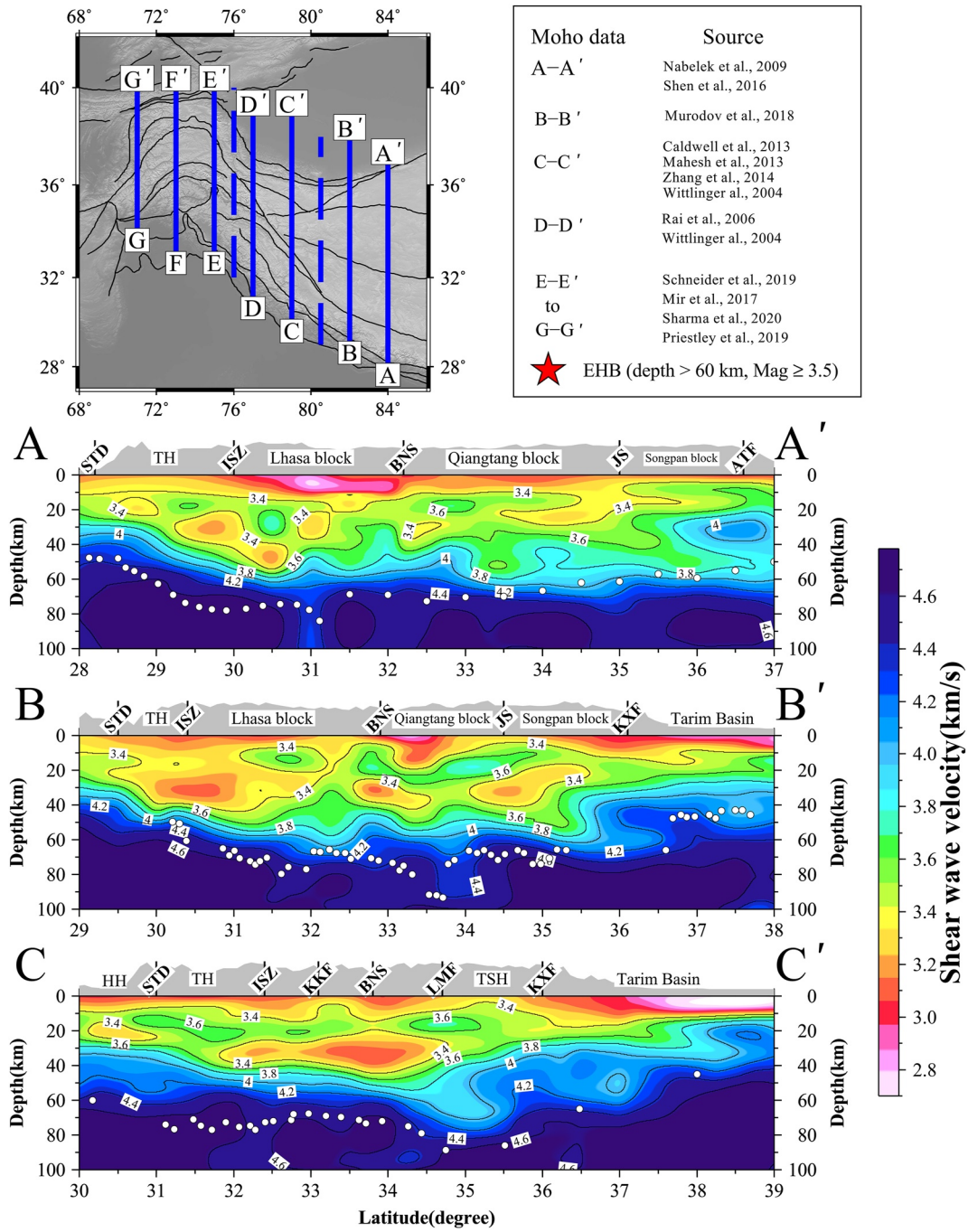

Figure 6. North-south velocity-depth sections along varying latitudes. The location of each profile (thick blue line) is given at the top left corner. The details of the sources providing the Moho data (white dots in each profile) are presented in the top right corner. Surface topography with positions of major tectonic blocks and faults are presented at the top of each profile. The color data indicate absolute shear wave velocities below sea level from depth 0–100 km. The black lines in each velocity profile indicate Vs contours at 3.4, 3.6, 3.8, 4.0, 4.2, 4.4, and 4.6 km/s. Two extra profiles (dashed blue lines at top right corner), one between B-B´ and C-C´ and other between D-D´ and E-E´ are presented in Figure S22 of Supporting Information S1.

We trace the characteristics of the HVLC in this work to infer the northern extent of the underthrusting Indian lower crust. The breadth between the 4 km/s contour and the Moho depth (marked as white dots in Figures 6 and 7) can be used to determine the thickness of the HVLC. Additionally, the north-south velocity profiles in Figures 6 and 7 are also shown with Vs contour lines showing the HVLC's geometry in Figure S21 of Supporting

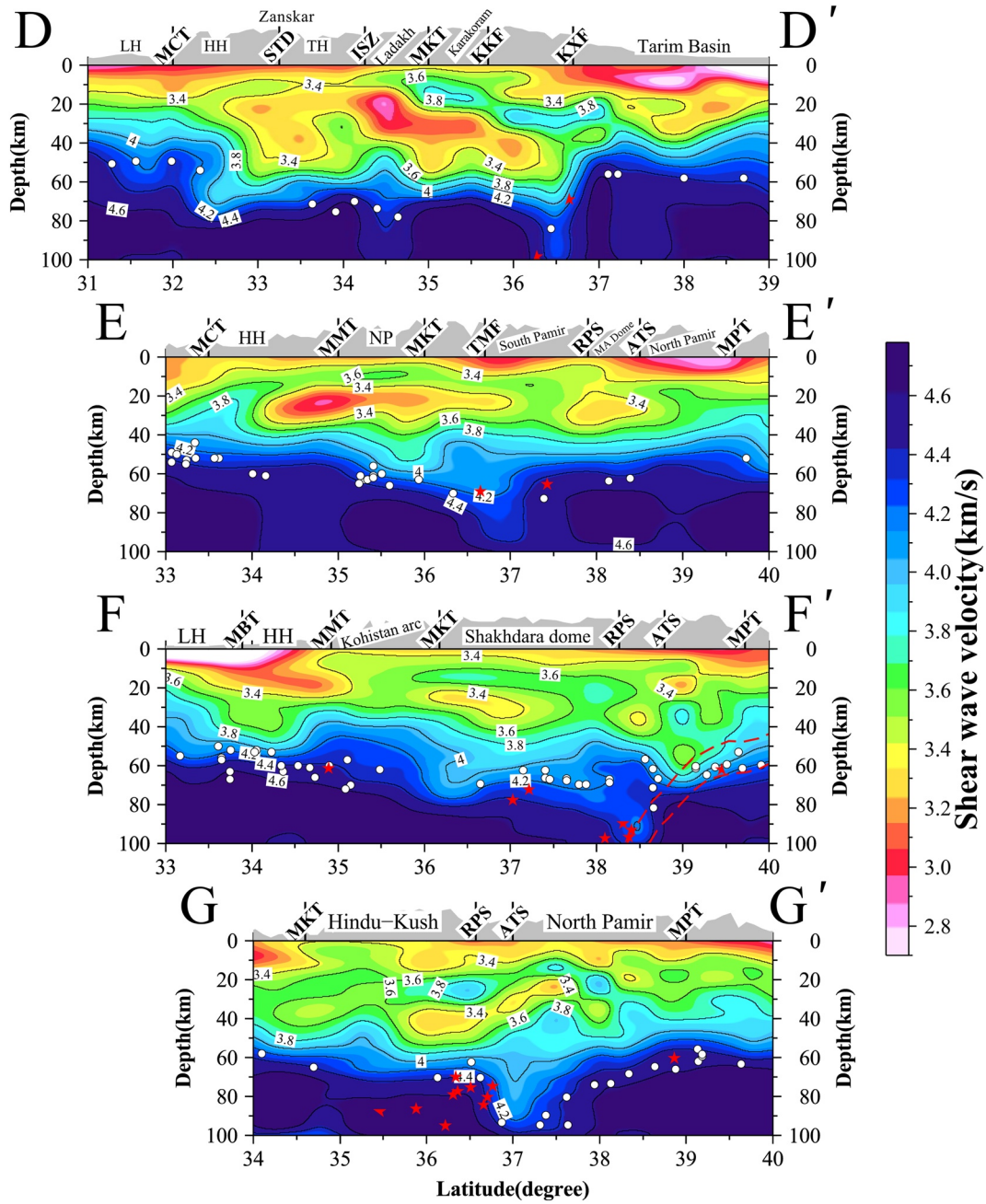

Figure 7. Same as Figure 6. The red stars indicate locations of earthquakes below 60 km obtained from the EHB catalog. The dashed red lines in profile F-F′ represent subducting lower crust of Pamir (Schneider et al., 2019).

Information S1. A shear wave velocity lower than 3.4 km/s (LVZs) is attributed to the presence of sediments and/or fluids (Yang et al., 2012).

Figure 6 (profiles A-A′ to C-C′) represents three velocity-depth sections from the high Himalaya to western Tibet-Tarim along 84°, 82°, and 79°E. The 84°E profile closely follows the Hi-CLIMB seismic line (Nábělek et al., 2009), re-investigated by Nowack et al. (2010) and Z. J. Xu et al. (2013). Nábělek et al. (2009) performed depth migration of RF data using a two-dimensional velocity model. In order to minimize the influence of interference from shallow layers, they combined the migrated PS conversions with the images of migrated PpS and PsS multiples to produce the final image, which enhances the wavefield to be coherent in all three images. The profile data was subjected to joint inversion of RF measurements with group and phase velocity dispersion data to

compute the crustal velocity model (Z. J. Xu et al., 2013). The Moho depth from the two approaches agrees very well, with a maximum variation of up to 5 km. Note that even in the joint inversion, the depth of the Moho determination is non-unique, particularly when it is gradational and depends on the Moho velocity considered. The Moho between 28−34°N and 34−37°N is taken from Nábělek et al. (2009) and Shen et al. (2016), respectively. Our velocity image has several notable features. The Moho depth computed using RF coincides with the shear wave velocity (Vs) increase of ∼4.4 km/s to ∼4.6 km/s in the Himalayas and southern Tibet (28–33.5°N), and a reduced velocity of ∼4.0 to ∼4.2 km/s in northern Tibet (33.5–37°N) as expected due to significant deformation and higher mantle temperature in northern Tibet (Molnar et al., 1993). In the LB, the Moho depth increases from ∼50 km beneath the STD to about 75–80 km till 31°N. Farther north, it is at a depth of 70 km, continuing till 33.5°N in the QB and at 60 km beneath the Songpan block. We observe a structural break in the upper mantle at 31°N, which is also correlated with the weak Moho converted phase in the RF of Nábělek et al. (2009). This complexity of the Moho has also been inferred by Z. J. Xu et al. (2013) between 31° and 33°N. The HVLC (7x layer between the contour of Vs ∼4 km/s and the Moho in the profile A-A′) is identified as a continuous north dipping feature (∼20 km thick) from the Tethys Himalaya to about 31°N (also see Figure S21 in Supporting Information S1). Between 31°N and 33°N, this layer flattens out with a thickness of ∼10–15 km. Farther north, beneath the northern QB and the Songpan block, the HVLC is significantly thin. Nábělek et al. (2009) imaged the continuation of the HVLC only till 31°N based on their CCP modeling and interpreted it to indicate the underplating of the Indian lower crust. In the middle crust at a depth of 20–50 km, we observe two prominent low-velocity pockets, one about 150 km long stretch of north dipping LVZ (Vs ≤ 3.4 km/s) across the southern LB (Gangdese batholith) and the other beneath the north QB at a depth of 10–25 km.

The velocity image along 82°E (Figure 6, profile B-B′) aligned with the ANTELOPE profile (Murodov et al., 2018; J. Zhao et al., 2010) shows a complex crustal structure. The Moho is imaged using H-κ stacking (Murodov et al., 2018) for data that clearly show Ps conversion along with the Moho multiple in the RF and is consistent with results of Gilligan et al. (2015), Z. Zhang et al. (2014), and J. Zhao et al. (2010). Along the ANTELOPE-1 profile, the crust and upper-mantle structure have been previously investigated using the *P* and *S* RF CCP migration method (J. Zhao et al., 2010) using the IASP91 global reference model for the conversion of differential times into depths. The obtained depths are relatively insensitive to absolute velocities because the differential times depend largely on velocity differences. Additional results from joint inversion of RF and surface wave dispersion for western Tibet covering 77-82°E (Gilligan et al., 2015) were used to ensure the reliability of the computed Moho depth. The Moho, with a velocity transition of ∼4.4–∼4.6 km/s, dips northward from 50 km below the High Himalaya to 80 km below the BNS at 33°N. Murodov et al. (2018) reported a 15 km upward offset in the Moho below northern Lhasa (at 32°N) and a depressed Moho up to 90 km below the central Qiangtang (at 33.5°N). In the Songpan block, the Moho is at a depth of 70 km (Vs transition of ∼4.4–4.6 km/s) and then abruptly shallows to 48 km (Vs transition from ∼4 to 4.3 km/s over a longer wavelength) beneath the Tarim Basin. Maceira and Ammon (2009) observed a Moho depth of 53 km and an uppermost mantle velocity of 4.3 km/s beneath the western Tarim, which is also corroborated by our results showing a gradational increase in Vs from 30 km depth (Vs ∼ 4.0 km/s) to 60 km depth (Vs ∼ 4.4 km/s) (at 36–38°N). The HVLC exhibits a complex geometry (also see Figure S21 in Supporting Information S1). A north dipping HVLC with a variable thickness (10–20 km) is observed between the Tethys Himalaya (29°N) and the southern QB (33.5°N). In the northern Qiangtang and Songpan blocks (33.5–35.5°N), the HVLC is nearly flat with a thickness of about 10 km. Across the KXF (∼36°N), the Vs ∼4.0 km/s contour exhibits a significant vertical offset of ∼20–25 km. Similar to the profile A-A´, we observe a thick LVZ (3.2–3.4 km/s) in the middle crust progressively deepening from about 20 km beneath the STD to 45 km at 32°N in the northern Lhasa. Two additional discrete and localized LVZs are also present beneath the Qiangtang (central Tibet) and Songpan blocks. However, we could not find any spatial continuity of the mid-crustal low-velocity packets between southern Tibet and northern Tibet in profiles along 84°E and 82°E (Figure 6, profiles A-A´ and B-B´).

The velocity section along 79°E (Figure 6, profile C-C´) has been earlier investigated by several researchers in individual segments from the Ganga Basin to STD (Caldwell et al., 2013; Mahesh et al., 2013), ISZ to LMF (Z. Zhang et al., 2014), and LMF to KXF with horizontal offsets (Wittlinger et al., 2004). These studies used CCP migration to map structural discontinuities in the crust and upper mantle. Except at the ATF, the Moho depth derived by Wittlinger et al. (2004) is in agreement with the joint inversion result of Gilligan et al. (2015). However, the Moho depth of Caldwell et al. (2013) beneath the Himalayas is shallower by 5 km as compared to the joint inversion result. The difference in the Moho depth between the CCP and joint

inversion is most likely due to the lower velocity (Vs > 4.0 km/s) considered by Gilligan et al. (2015) to represent the Himalayan Moho as compared to Vs > 4.4 km/s. We used the Moho depths inferred from these experiments to constrain the nature of the lower crust. Between 35°N and 37°N (approximately between LMF and KXF), the HVLC is significantly thick (~30–40 km). The Moho corresponds to the shear velocity transition of ~4.4–4.6 km/s except near the KXF and Tarim Basin, where the Vs changes from ~4.2 to 4.4 km/s. Two distinct low-velocity layers (Vs < 3.4 km/s) are present in the middle crust. The southern one, at 20 km depth, is between STD and MCT in the high Himalaya with a thickness of 10 km, while the other is nearly horizontal from the ISZ to LMF with a varying thickness of 10–20 km. The low-angle north dipping HVLC is ~25 km thick (depth from 35 km to the Moho at 60 km) beneath the high Himalaya, progressively decreasing to about 15 km between the LMF and KXF, where the Moho is 80 km deep. In the vicinity of the KXF and farther north, we observe a sharp decrease in the Moho depth. It reaches to 60 km at the KXF and 45 km in the Tarim Basin at 38°N.

The velocity profile along 77°E (Figure 7, profile D-D´) represents the contact between the western and central Himalaya in the south, and western Tibet and the Pamir in the north. It also represents a change in the nature of the production of granites and the subduction behavior of the India plate. East of 77°E, the hanging wall of the MCT has high-grade metamorphic rocks of the Greater Himalayan Crystalline (GHC), whereas, west of 77°E, the MCT juxtaposes low-grade rocks of the GHC and LH (Yin, 2006). Furthermore, significant segmentation of the Indian lithosphere is proposed to occur across this boundary (Hetényi et al., 2016). The profile presents a complete section of the India-Ladakh-Asia convergence with a well-preserved deformation history of the Indian plate in the strongly deformed Tethyan passive margin platform and Zanskar's shelf sedimentary rocks (Corfield & Searle, 2000). The velocity profile along 77°E is shown in Figure 7 (profile D-D´). The Moho depth is taken from the joint inversion result of Rai et al. (2006) from the Ganga Basin to the Karakoram and CCP migration results (Wittlinger et al., 2004) farther north. The HVLC (7x layer) of 15 km thickness above the Moho at 50 km depth flexes northward at MCT to the Zanskar shear zone (STD equivalent). The large offset in the 4.0 km/s velocity contour at 32.5°E is probably an indication of lateral variation in the Himalayan geology (around 77°E) discussed earlier. From Zanskar to Ladakh and the Karakoram, the HVLC is identified between 60 and 75 km, although the Moho from RF analysis is sparsely determined here. The Moho deepens from 50 km beneath the MCT to about 70 km beneath the Tethys Himalaya and Ladakh and 80 km beneath the KXF. Farther north, the Moho thins to 60 km with a large vertical offset in the Tarim Basin, accompanied by about 20 km of the HVLC. We find LVZs between 20 and 50 km depth beneath the Zanskar-Ladakh-Karakoram zone, with the lowest velocities (Vs < 3.2 km/s) beneath the Ladakh zone. The LVZs appear to be connected in the upper crust (~20 km depth), but they are likely separated below 30 km depth by a north-dipping zone (Vs ~ 3.4 km/s) beneath the Zanskar and the another (Vs 3.0–3.4 km/s) beneath the Ladakh and Karakoram. Across the KKF, no significant changes in the crustal structures (i.e., offsets in the mid-crustal low-velocity zones or HVLC) are observed. However, the KXF (~36.5°N) marks the zone of deep seismicity and large vertical offsets in crustal structures.

The velocity sections along 75°E, 73°E, and 71°E (Figure 7, profile E-E´, F-F´, G-G´) represent the convergence of the western India-Kohistan plate with the Asian plate (Karakoram-Pamir-Hindu Kush). The crustal structure in the Pamir and Hindu Kush has been extensively studied by RF approach (Schneider et al., 2019), joint inversion (W. Li, Chen, Tan, & Yuan, 2020), and tomographic studies (W. Li et al., 2018). In the western Himalayan syntaxis-Kohistan region, the Moho depth is adapted from Mir et al. (2017) and Sharma et al. (2020) based on joint inversion of RF and surface wave data. Also, we included data from the Pakistan National network, Nanga Parbat network, and Pakistan Himalaya network presented in Priestley et al. (2019). We use the Moho depths and the nature of the subducting Asian lower crust inferred from these studies to discuss our results in profiles E-E´, F-F´, and G-G´ of Figure 7. Along 75°E (E-E'), the Moho depth, with a Vs transition of 4.3 to >4.4 km/s, varies from 50 km beneath the Lower Himalaya to 70 km beneath the southern Pamir at 37°N. Farther north, it progressively decreases to 50 km beneath the Main Pamir Thrust (MPT). The HVLC continues uninterrupted from the MCT in the south to the MPT in the north, except for a localized ~100 km wide flexing at 37°N, where deep earthquakes are observed (also see Figure S21 in Supporting Information S1). Two prominent LVZs extending to a depth of 20–40 km are mapped along the profile: the first one from 34°N to 37°N between the ISZ/MMT and the Tirich Mir Fault, covering the Ladakh arc-Nanga Parbat-Karakoram batholith and its northward extension; and the second below the surface exposure of the gneissic dome (e.g., Muztagh Ata dome) in the central and eastern Pamir between the RPS and ATS.

The velocity structure along 73°E (F-F´) from the Pakistan Himalaya to the north Pamir crosses two major geologic terrains– the Kohistan arc and the SD. The Moho depth increases from 50 km below the lower Himalaya to about 70 km at the MMT, represented by a Vs transition of ∼4.3–4.6 km/s. Below the Kohistan arc, the 7x layer (HVLC) is significantly thick (25 km) at a depth of 35–60 km, suggestive of an unstable lowermost crust that could detach in the future, leading to the evolution of a more felsic continental crust (Jagoutz & Kelemen, 2015). In the Pamir, the Moho is at an average depth of 60 km and characterized by a reduced Vs transition of 4–4.2 km/s, suggesting a higher mantle temperature. A Moho doublet and deep seismicity with a large flexure of the HVLC are observed in the central Pamir at ∼38.5°N. Schneider et al. (2019) interpreted this complex feature as a result of subducting Asian lower crust that got detached beneath the central Pamir (dashed red lines, adopted from Schneider et al. [2019], in profile F-F´). A mid-crustal (20–40 km depth) low-velocity domain is mapped in the south Pamir beneath the SD. Note that the LVZ does not reach the surface. The presence of the LVZs in the depth range of 20–40 km beneath the high-grade gneiss domes is also supported by local earthquake and surface wave studies (W. Li et al., 2018; Sippl et al., 2013). These high-grade gneiss domes were formed by large-scale crustal extension that resulted in the exhumation of mid-crustal material (from 30 to 50 km depth) to the surface of the Pamir (Hacker et al., 2017), and they have a geothermal gradient of ∼40°C/km that would lead to melting temperatures >700°C below ∼20 km for most of the crustal rocks observed here as LVZs. At the southern extremity of the profile, the Peshawar Basin (33–35°N) in the western Himalaya is characterized by low velocity to a depth of ∼20 km.

The westernmost velocity section along 71°E runs from the Main Mantle Thrust/ISZ in Pakistan to the Hindu Kush and the western end of the Pamir Plateau. A mid-crustal low-velocity layer is mapped from 36° to 38°N beneath the gneiss domes located in the west part of the southern and central Pamir. The Moho depth ranges from 60 to 70 km beneath the Hindu Kush, with a nearly flat (∼10 km thick) HVLC between 34°N and 36.5°N. In contrast, a south dipping Moho, from ∼60 km beneath the north Pamir (across the MPT) to ∼90 km beneath the west-central Pamir (between the RPS and ATS), is observed between 37.5°N and 40°N. Similar to the Profile F-F´ discussed earlier, a significant flexure of the HVLC at 37°N correlates with the previously identified Moho doublet of Schneider et al. (2019) and the deep focus earthquakes (depth >100 km) shown in Kufner et al. (2016, 2017). Between 37.5° and 40°N, the Moho is south dipping, with a depth of ∼60 km near the MPT to ∼95 km at the ATS. This south dipping Moho is also associated with the south dipping HVLC (∼10–25 km thick, also see Figure S21 in Supporting Information S1), probably indicating the southward subducting Asian lower crust shown in Schneider et al. (2019).

7. Discussion

Here, we discuss the geodynamic implications of the crustal velocity model of this study. Because of the inclusion of a large number of new data, we can present a comprehensive 3-D shear velocity model of the crust beneath the west and northwest segment of the India-Asia convergence zone, comprising western Tibet-Ladakh-Kohistan-Pamir-Hindu Kush, western Himalaya, and adjoining basins. We make three significant observations that provide new insights into the nature of the crustal fabric and tectonics of the region. These results are summarized in Figure 8 and discussed below.

7.1. Northern Limit of Indian Lower Crust Beneath the Tibet-Karakoram-Pamir

Evidence for the Indian plate crust underplating Tibet and the Pamir typically comes from the findings of faster lower-crustal material (Wittlinger et al., 2009), well-developed shear zones beneath the Himalayas (Schulte-Pelkum et al., 2005), and deep crustal earthquakes (Priestley et al., 2008). In eastern Tibet, deep earthquakes and fast seismic wave velocities at the bottom of the Tibetan crust signify the eclogitization of the lower crust of India (Huang et al., 2009; Monsalve et al., 2008). In southern parts of central and western Tibet, using seismic evidence for multiple impedance contrasts in the crust (or observing intra-crustal layers), Nábělek et al. (2009), Schulte-Pelkum et al. (2005), and Z. J. Xu et al. (2017) reported the presence of eclogitized Indian crust underthrusting at least the northern LB. These studies show (a) a crustal positive amplitude arrival, seen at all Tibetan stations at depths of 45–55 km, implying a high-velocity layer in the lower crust, and (b) at the same stations, conversions from the Moho are weaker than those observed over the Nepal Himalaya, which is expected for a reduced velocity contrast at the Moho due to a fast lower crust. The detailed analysis using earthquake travel-time data requires a fast lower crust under the southern Tibetan plateau, with P velocities of over 7.0 km/s. This cannot be explained by increased

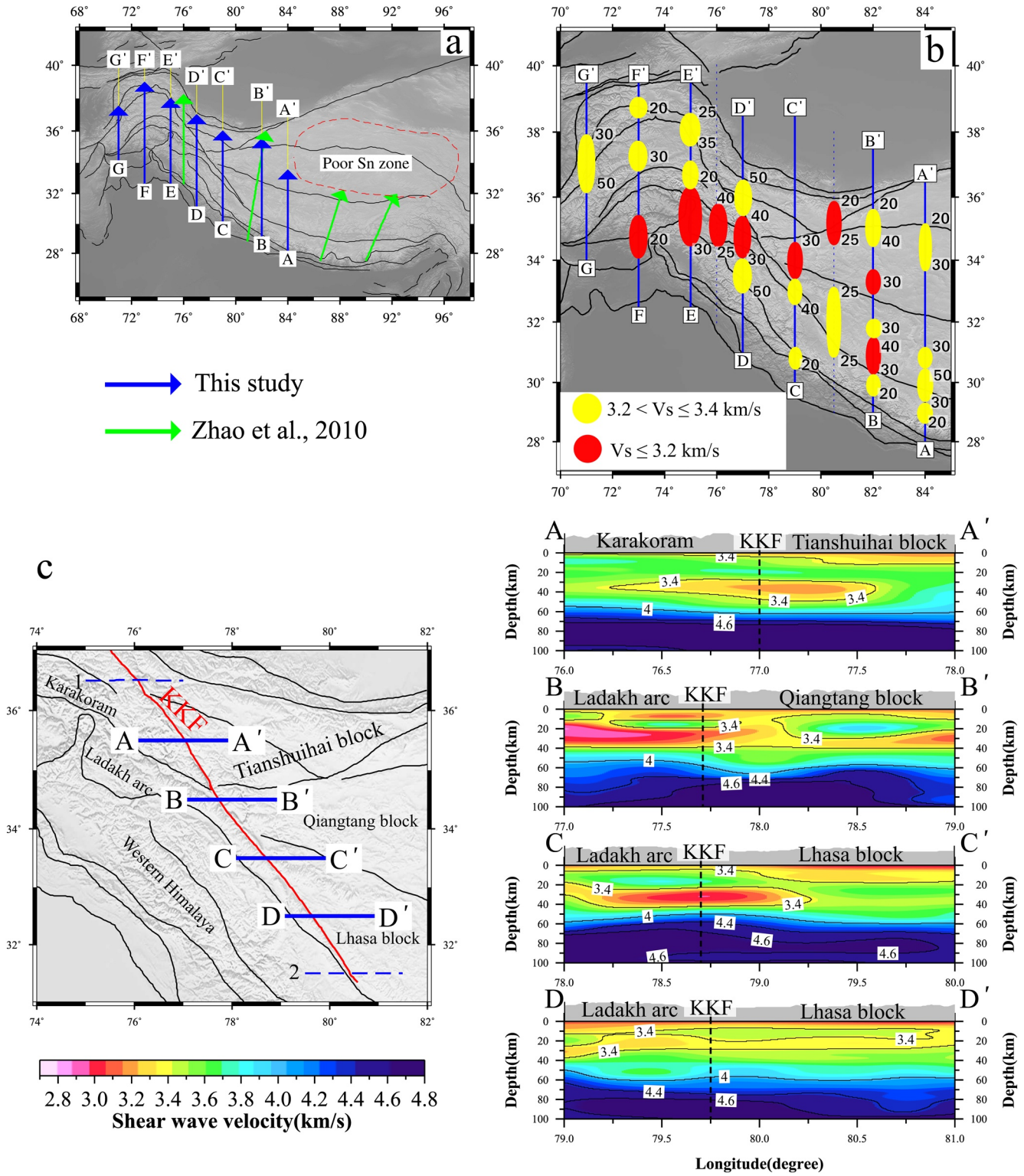

Figure 8.

pressure due to the deep burial of the Indian crust. It is often modeled as an anomalous velocity increase due to partial (30%) eclogitization of the lower Indian crust (Schulte-Pelkum et al., 2005).

Wittlinger et al. (2004) observed large offsets in the Moho and crustal structures near the KXF and interpreted the southward underthrusting of the Tarim lithosphere under the northwestern Tibet-Kunlun. Further west,

observations of deep seismicity, high-velocity intra-crustal layering, and the Moho doublets have been used to delineate the geometry of the subducting Asian lower crust under the Pamir and the Hindu Kush (W. Li et al., 2018; Schneider et al., 2019; Sippl et al., 2013).

The studies mentioned above used the geometry of the HVLC and provided evidence for the northward underthrusting of the Indian crust under Tibet and the southward subduction of the Asian crust under the Pamir and western Kunlun. While the geometry of the subducting Asian crust has become more evident in recent years (W. Li et al., 2018; Schneider et al., 2019), the fate of the underthrusting Indian crustal front beneath western Tibet-Karakoram and the Pamir remains poorly understood. Priestley et al. (2008) combined the results from the previous studies with the depths of moderate-size earthquakes at the northwestern edge of the plateau to argue for the presence of the cold, dry granulite-rich crust of India beneath most of western Tibet. L. Li, Murphy, and Gao (2020) reported the presence of strong radial anisotropy in the crust and upper mantle beneath western Tibet, and mapped the underthrusting Indian lower crust limited to the region north of the KKF. However, other seismic velocity studies in west Tibet (e.g., Griffin et al., 2011; Razi et al., 2014) failed to detect high seismic velocity in the lower crust. By mapping deep seismic discontinuities under Tibet, J. Zhao et al. (2010) observed low-angle underthrusting of the Indian plate beneath the entire western Tibet, in contrast to eastern Tibet. The discrepancy in the geometry of the Indian lower crustal front in western Tibet obtained from these studies is probably due to inadequate lateral resolution, such as ∼150 km in the tomographic image of L. Li, Murphy, and Gao (2020).

As discussed earlier, the HVLC represents various processes such as magmatic addition to the crust, magmatic differentiation, accretionary tectonics, and the transformation of the mafic lower-crustal rocks into eclogite or garnet granulite (Schulte-Pelkum et al., 2017). In the case of the Himalayas and southern Tibet, this HVLC is interpreted as the underthrusting Indian lower crust that may be partially eclogitized (L. Li, Murphy, and Gao (2020); Nábělek et al., 2009; Schulte-Pelkum et al., 2005). We map the continuity of this HVLC from the Himalayas to farther north in Tibet and the Pamir, and use the observations of the Moho doublets, large structural offsets across major fault boundaries, and deep seismicity (discussed in the previous section) to define the northern limit of the Indian crust under western Tibet-Karakoram and the Pamir region. Figure 8a depicts the extent of HVLC from the Himalayas in the south to varied latitudes in western Tibet and the Pamir. As discussed in Section 6.2 earlier, the velocity profiles from A-A´ to D-D´ (Figures 6 and Figure 7) constitute the western Himalaya-western Tibet-Kunlun and Ladakh regions. Along profile A-A´ (84°E), continuity of ∼20 km thick fast velocity lower crust from Tethys Himalaya to southern QB (33°N) represents the Indian crustal front (also see Figure S21 in Supporting Information S1). Farther north, the thickness of HVLC is insignificant. The crustal velocity in profile B-B´ shows a complex Moho (31–33°N), probably indicating the consequence of the Indian lower crust that got decoupled from the underlying subducting lithosphere at 31°N and moved farther north with the overlying crust. Additionally, profiles B-B´ to D-D´ (between 82°E and 77°E) show significant changes in the crustal structures in the vicinity of the KXF at the western end of the ATF. The most prominent characteristic is the depth offset of the 4 km/s contour in the proximity of the KXF. Also, we observe about 20 km of shallowing of the Moho across the KXF. The fault also marks the zone of deep earthquakes (Figure 7, profile D-D´). Based on the above structural changes in the crust, we believe the KXF marks the boundary in northwestern Tibet where the Indian crust and Asian crust meet and jointly deform, producing deep-seated earthquakes consistent with previous studies (Priestley et al., 2008; J. Zhao et al., 2010). In the Pamir-Hindu Kush-Karakoram regions, flexure of the HVLC resulted in the thicker lower crust, the Moho doublets, and the deep seismicity beneath the south-eastern Pamir (at 37°N in velocity profile E-E´) and the central to west-central Pamir (between RPS and ATS in profiles F-F´ and G-G´) and define the zone of interaction between the northward underthrusting Indian lower crust and the southward subducting Asian crust. The high-velocity lower crust in the Pamir is interpreted as a seismic response of gradual eclogitization of subducting crustal materials, a view supported by the

Figure 8. (a) Possible northern limit of the Indian crust along the six velocity profiles (Figure 6) based on the nature of velocity of lowermost crust (7x layer) represented by the breadth between shear velocity of 4.0 km/s and the Moho. Blue lines represent results of this study and green lines are of J. Zhao et al. (2010). The arrowheads indicate the northern limit. The red dashed polygon shows a zone of the low-velocity upper mantle in northern Tibet (J. Zhao et al., 2010). (b) Spatial distribution of low-velocity anomalies in the middle crust between 20 and 50 km depth. The position and size of each anomaly (shown as red and yellow ellipses) is determined by examining the Vs ∼ 3.4 km/s contour of each north-south velocity profile of Figures 6 and 7. The depth (in km) of the base of the low-velocity layer is also presented next to each anomaly. The velocity profiles corresponding to the dashed blue lines are presented in Figure S22 of Supporting Information S1. (c) Velocity-depth profiles (blue lines in left panel) across the Karakoram Fault (red line in left panel) are presented in the right panel showing a continuation of velocity signature and the depth extent of fault (<20 km). The gray shaded area in velocity profiles shows surface topography. The vertical dashed back line in each profile shows the approximate position of the KKF. The black lines are velocity contours. Two extra east-west profiles shown as blue dashed lines (1, 2) are shown in Figure S23 of Supporting Information S1.

presence of eclogite and other high metamorphic rocks in the crustal xenoliths (Hacker et al., 2005), RF (Schneider et al., 2019), and tomographic studies (Kufner et al., 2017; Sippl et al., 2013). Our result of the Indian crustal front in western Tibet and the Pamir combined with J. Zhao et al. (2010) shows that the Indian lower crust underthrusts Tibet and the Pamir up to varying latitudes (Figure 8a). In eastern Tibet, only southern Tibet is underthrusted by the Indian crust. However, in central and western Tibet, it reaches farther north beyond the Qiangtang and Tianshuihai blocks than its previously assumed boundary in the LB (e.g., L. Li, Murphy, & Gao, 2020; Nábělek et al., 2009). In the Pamir-Hindu Kush, the possible northern limit of the Indian crustal front lies in the central Pamir between the RPS and ATS.

7.2. Mid-Crustal Low Velocity and Its Lateral Variation

Since the early geophysical observations of significant *P* wave velocity decrease in the upper/middle crust of the Tibetan Plateau (L. D. Brown et al., 1996; Nelson et al., 1996), numerous geophysical studies followed to examine its plateau-wide distribution, depth control, geological explanation, and its role in the making of the plateau (Agius & Lebedev, 2014; Caldwell et al., 2009; Gilligan & Priestley, 2018; Hetényi et al., 2011; Klemperer, 2006; W. Li et al., 2018; Rippe & Unsworth, 2010; Searle et al., 2011; Yang et al., 2012). Corresponding high conductivity zones at a mid-crustal level have also been reported in southern Tibet (Bai et al., 2010; Unsworth et al., 2005), northwest Tibet and the Himalayas (Arora et al., 2007), and the Pamir (Sass et al., 2014) which further supports fluid rich, weak middle crust throughout the orogenic belt. These studies suggest that the underthrusted Indian crust below about 20 km depth, forming the present-day Tibetan middle crust, is partially molten. Therefore, it is susceptible to southward flow in response to the gravitational potential energy gradient between Tibet's weak middle crust and the eroding Himalayan front (summaries in Hodges, 2006; Klemperer, 2006). The above observations led to the suggestion of ductile flow in Greater Himalayan Sequence (GHS) rocks, continuity in the subsurface beneath the northern Himalayan thrust belt and molten middle crust of Tibet, and the evolution of the controversial concept of channel flow in the Himalayan-Tibetan orogenic system (Grujic et al., 1996, 2002; Jones et al., 2006; Law et al., 2004). The channel flow model was introduced to explain the apparent partially molten Tibet's middle crust that is extruded southward by buoyancy forces acting on the elevated Tibetan crust. This process, which has been active at least since the early Miocene, has a surface manifestation in the early to mid-Miocene rocks produced from mid-crustal melts and now found at the surface between the MCT and the STD as leucogranites.

The early controlled source seismic data have been supplemented by networks of broadband seismographs as linear arrays or spread over the region, and a few MT investigations provide evidence for conducting middle crust coinciding with LVZs. The surface wave tomographic images of Gilligan and Priestley (2018) and Yang et al. (2012) suggest the continuous presence of low velocities (Vs $\sim$ 3.2–3.4 km/s) in the middle crust of Tibet at a depth range of 20–40 km. Both studies have limited spatial resolution. The study of Yang et al. (2012) is primarily confined to the east of 80°E with a horizontal resolution of 150–200 km. Gilligan and Priestley (2018) could resolve features of 3° × 3° or more for periods of more than 10 s. Using high-density RF data, Hetenyi et al. (2011) proposed the existence of discontinuous low-velocity channels of a horizontal length of about 50 km. Due to the non-continuity of LVZs and the observation of a regular crustal mean Vp/Vs ratio, Hetenyi et al. (2011) questioned the widespread existence of partial melt in southern Tibet and, hence, the channel flow model. The regional presence of LVZs and conductors in the crust may be due to graphite, mica, fluids, partial melts, aqueous fluids, high intra-crustal heat production (radiogenic, shear heating) or a combination of these, and are easily capable of producing an observed wave velocity decrease of 7%–17% (Takaei, 2000). The LVZ may also represent strong radial anisotropy in the middle crust (L. Li, Murphy, & Gao, 2020; Shapiro et al., 2004). Existing seismological images do not have the adequate horizontal resolution to establish subsurface linkage of possible LVZs within Tibet extending southward to the GHS in the Garhwal Himalaya, where leucogranites are exposed on the surface with a root of about 10–15 km (Ashish et al., 2009), or in the western Himalaya. The availability of newer data helps us develop better-resolved velocity images and examine the existence of such an LVZ in the hitherto poorly explored regions of west Tibet-Himalaya and the Ladakh-Pamir-Hindu Kush. We can resolve the target of 50 × 50 km which is at least three times better than the existing seismic velocity images.

First, we quantify the amplitude of low-velocity at mid-crustal depths for an undeformed crust. A solid, dry metamorphic rock at ~1,000 MPa (~30 km) has an average shear wave velocity of ~3.65 km/s at room temperature

(Christensen, 1996). Under the influence of temperature, the rock will begin to melt at a temperature >900°C (Litvinovsky et al., 2000), leading to a reduced velocity of 3.4 km/s considering a 0.2 m/s/°C decrease in velocity (Kern et al., 2001). It is further reduced in the presence of water and hydrous minerals. Wang et al. (2016) presented evidence for 8%–22% partial melts from central and northern Tibet constrained by estimates of Rb/Sr in the source from Nd and Sr isotopes and REE contents of the Pliocene-Quaternary lavas. While such estimates of 8%–22% are consistent with the MT data in Tibet (Unsworth et al., 2005), they are higher than the melt fractions (1%–7%) suggested by many seismic studies (Caldwell et al., 2009).

Like Yang et al. (2012), we also use a reference velocity of Vs ≤ 3.4 km/s as an indicative of LVZs. We focus here on examining how widespread is the distribution of mid-crustal LVZs in the region by investigating their spatial distribution. Earlier, we have shown that low-velocity layer anomaly of up to 3%–5% and thickness 5 km could be best recovered (Figure S15 in Supporting Information S1). The *S*-velocity maps at different depths (Figure 5) suggest the presence of low-velocity primarily confined to 20–40 km depth. The anomaly may be laterally averaged and smoothed during velocity contouring. To investigate the distribution of the LVZs, we examine their depth distribution along the N-S velocity profiles of Figures 6 and 7, along with a few more shown in Figure S22 of Supporting Information S1.

The distribution of mid-crustal low-velocity domains (between 20 and 50 km depth) along with their maximum depths (the approximate bottom of the layer) is presented in Figure 8b. The low velocities could be broadly classified into regions with Vs ∼ 3.0 to <3.2 km/s and 3.2–3.4 km/s. The LVZs are discontinuous and exist in patches with no specific distribution of coherent depth and velocity amplitude from south to north Tibet as required for continuous flow channels (Clark & Royden, 2000). In the Pamir region, the LVZs in 20–40 km depth correlate well with the surface distribution of gneiss domes where a large-scale extension is proposed at 30–50 km depth (Hacker et al., 2017; Schurr et al., 2014). A similar low-velocity layer is mapped at a depth of 30–50 km in the GHS beneath the western Himalaya (77°E, Figure 7, profile D−D'), continuing further north to the Ladakh and Karakoram batholiths. We also observe relatively continuous LVZs extending from southern Tibet to the STD, suggesting that E-W extension in Tibet is transferred southward to the central and western Himalaya (Hintersberge et al., 2011). While the discrete mid-crustal LVZs in south-east Tibet partially correlate with surface grabens (Hetenyi et al., 2011), no such correlation is observed in western Tibet.

Though the low velocities due to crustal melts are widely present in the study region encompassing the western Himalaya, western Tibet, and the Pamir, their generic linkage to a common source remains an open question. The absence of a coherent 3-D LVZ suggests that the complexity of this region is a result of mechanical deformation along with magmatic activity (Tseng et al., 2009) and could be correlated with broad extensional regime within Tibet (Gan et al., 2007), the localized collision-parallel extension in the southernmost Tibet and northern Himalaya (Styron et al., 2011), presence of the localized low-velocity horizon in the western Himalaya (Caldwell et al., 2009) or decompressive melting beneath the gneiss domes in the Pamir, western Himalaya, Karakoram, and the Garhwal Himalaya. The observed disconnected LVZs agree with the results of Hetenyi et al. (2011), and suggest that the channel flow model is not a valid proposition, particularly with reference to its applicability in the western Himalaya-western Tibet and the Pamir region. It may be recalled that the proponents of the channel flow model for eastern Tibet did not apply the model to the southern Himalayan margin, but argued that the crustal thickening could be explained there by upper crustal shortening accommodated by folding and faulting (Clark & Royden, 2000). It has been argued that heating related to crustal thickening drives crustal melting, reduces the crust's strength, and causes orogenic collapse. Several tectonic and surficial processes may lead to near-isothermal decompression of the deep crust. Other mechanisms that could generate partial melt include extension, decompression via removal of the upper crust, crustal thinning, and diapirism. Our velocity image uses vertically polarized wave (Vsv) obtained from Rayleigh wave analysis. The addition of Love wave data may further help in understanding whether the decreased wave velocities in the middle crust depend on composition, temperature, and partial melts (if any) or whether, they represent preferential alignment of anisotropic minerals (e.g., Agius & Lebedev, 2014; L. Li, Murphy, & Gao, 2020; Shapiro et al., 2004).

7.3. Depth Extent of the Karakoram Fault (KKF)—Does It Interrupts the Mid-Crustal LVZ?

The NW-SE trending right-lateral KKF from the northeastern Pamir to the Kailas region of southern Tibet marks the western flank of Tibet. It has been of interest to many researchers after Molnar and Tapponnier (1975)

first proposed the eastward extrusion of thickened Tibetan crust due to the northward indenting Indian crust. The extruding crust is bounded by the ATF in the north and the KKF along the southwestern margin of Tibet. The process of extrusion requires these faults to be lithospheric-scale structures with large horizontal motions (~500–1,000 km; Molnar & Tapponnier, 1975). While the ATF is at least a crustal-scale fault (Searle et al., 2011), the depth extent of the KKF is debated.

Based on relatively less abundance and age of old leucogranites (>18 Ma) west of eastern termination of the KKF, results of seismic and MT studies crossing it, and presence of high helium isotopic value indicating mantle fluid along the KKF, Klemperer et al. (2013) and Leech (2008) argue that the KKF penetrates deep into the crust and stops northward underthrusting of the Indian crust, thereby serving as a barrier to the crustal flow entering to the west in Himalaya and Ladakh. This conclusion would be correct even if the fault reached only halfway through the crust (Searle et al., 2011). Murphy and Copeland (2005) infer the mid-crustal reach of the KKF from the burial depths of rocks exposed by the associated normal fault. The knowledge of the depth extent of the KKF and its capability to generates significant shear heating are vital to understand the fault's role in crustal deformation and material transfer. A mid-crustal flow necessary for the plateau-wide outward expansion will preclude any surface faults from reaching deep into the crust. Limited seismological and MT studies show low shear wave velocity and high conductivity under Ladakh-Karakoram and western Himalaya, suggesting the continuity of mid-crustal LVZ south of KKF (Caldwell et al., 2009; L. Li, Murphy, & Gao, 2020; Rai et al., 2009). Gilligan et al. (2015) could not see any significant offset of mid-crustal LVZ along the fault and suggested that KKF does not cut through the entire crust. Due to inhospitable terrain on the international boundary, no geophysical experiment has been performed across the fault, and the above hypotheses on the depth extent of the KKF are yet to be resolved conclusively. Initial results suggested a high late Quaternary slip rate (30–35 mm/yr) on KKF (Avouac & Tapponnier, 1993), in contrast with recent GPS geodetic measurements suggesting a much lower rate of 3–5 mm/yr (E. T. Brown et al., 2002; Jade et al., 2004).

With a focus on resolving whether the KKF interrupts the mid-crustal flow from entering the western Himalaya and Ladakh, we generated several velocity-depth sections across the fault from its southern to its northern edge to examine the seismic velocity continuity (Figure 8c). Considering that our velocity model adequately captures the contrasting crustal structures across the crustal-scale KXF (western end of the ATF) (Figures 6 and 7), the response of the KKF would be visible in terms of significant vertical offset in mid-crustal LVZs or HVLC if it cuts deep into the crust. The four E-W trending velocity sections (Figure 8c, and two more in Figure S23 in Supporting Information S1) across the fault show continuity of mid-crustal LVZs in the depth range of 20–40 km without vertical offsets. No significant variation in the HVLC layers across the fault is observed. Therefore, the fault is mainly an upper crustal feature and may not play a significant role in crustal shortening. This view is also supported by micro geodynamic modeling of the fault's behavior in Wallis et al. (2014), and cross-sections based on shortening estimates across the NW Himalaya-Karakoram in Searle et al. (2010), suggesting that the KKF may be restricted to within the crust.

8. Conclusions

We investigate the crustal structure of the western Tibet-Pamir and the adjoining Himalaya-Ladakh region using a significantly improved shear wave image with the best resolution to a depth of 70–80 km. The velocity model with a horizontal resolution of 50 km has brought new insights into the tectonics of the region, summarized in Figures 6–8 and discussed below:

1. Our velocity image, combined with the Moho depth compiled from published studies, reveals the crust-mantle boundary beneath the Himalayas and south Tibet as a zone with a shear wave velocity transition of ~4.4 to ~4.6 km/s, and a reduced velocity of ~4.0 to ~ 4.2 km/s in northern Tibet and the Pamir. The Moho depth increases from 50 km in the Himalayas to 80 km below the BNS. There are marked E-W variations in lower crust complexity in western Tibet between 31° and 33°N. Beneath the Pamir, the Moho is at 70–80 km with an extreme of 90 km in the western part at 37°N.
2. Using the Moho depth and the nature of high-velocity lower crust (Vs > 4.0 km/s), we map the northern limit of the Indian crust extending farther north beyond the QB in the western Tibet (77–82°E) distinct from the previously thought boundary in the LB, and till the central Pamir in the western part of the India-Asia collision zone.

3. Mid-crustal laterally discontinuous LVZs (Vs $\leq$ 3.4 km/s) in the upper and middle crust exist in western Tibet. In the Pamir, the LVZs correlate with the surface distribution of gneiss domes. The inferred geometry of the LVZs do not provide support for a pervasive ductile channel flow model in western Tibet, the western Himalayas, and the Pamir region.
4. The study suggests that the KKF is an upper crustal feature due to the existence of uninterrupted LVZs beneath the fault at a depth beyond 20 km. The shallow depth extent of the KKF along with a much lower slip rate of 3–5 mm/yr suggests that the fault does not play an important role in crustal shortening during India-Asia convergence.

Data Availability Statement

The majority of waveform data for this study were downloaded from the IRIS DMC (https://ds.iris.edu/ds/nodes/dmc/) and GEOFON data center (https://geofon.gfz-potsdam.de/waveform/archive/). The seismic waveform data of ambient noise correlations and earthquakes, including their dispersion measurements, and the 3-D shear velocity model are provided as supplementary data. The Trans-dimensional tomography software can be downloaded from https://zenodo.org/record/4916124#.YMDWLS0Rrq0.

Acknowledgments
The research was supported by the Department of Science and Technology through the INSPIRE research fellowship to V.K. and J.C. Bose National fellowship to SSR. T.B. and R.H. are funded by the European Union's Horizon 2020 research and innovation program under grant agreement 716542. SSR had many valuable discussions with Peter Molnar, Vinod Gaur, Mike Searle, Keith Priestley, and Simon Klemperer that helped improve understanding of the Himalayan geodynamics. The authors thank Martin Schimmel for advice and discussion on the phase cross-correlation approach. The manuscript benefited immensely from the suggestions and critical review of associate editor P.G. DeCelles and two anonymous reviewers. The seismic waveform data provided by the IRIS DMC (https://ds.iris.edu/ds/nodes/dmc/) and GEOFON data center (https://geofon.gfz-potsdam.de/waveform/archive/) are highly appreciated. The generous support of the National Geophysical Research Institute (NGRI), Wadia Institute of Himalayan Geology (WIHG), and CSIR-4PI in using the seismological waveform data from their experiments is gratefully acknowledged. All figures were prepared using the GMT software (Wessel et al., 2013).

References

Acevedo, J., Fernández-Viejo, G., Llana-Fúnez, S., López-Fernández, C., & Olona, J. (2019). Ambient noise tomography of the southern sector of the Cantabrian Mountains, NW Spain. *Geophysical Journal International*, *219*(1), 479–495. https://doi.org/10.1093/gji/ggz308

Acevedo, J., Fernández-Viejo, G., Llana-Fúnez, S., López-Fernández, C., & Olona, J. (2021). Upper-crustal seismic anisotropy in the Cantabrian mountains (north Spain) from shear-wave splitting and ambient noise interferometry analysis. *Seismological Society of America*, *92*(1), 421–436. https://doi.org/10.1785/0220200103

Acton, C. E., Priestley, K., Gaur, V. K., & Rai, S. S. (2010). Group velocity tomography of the Indo-Eurasian collision zone. *Journal of Geophysical Research: Solid Earth*, *115*(B12), B12335. https://doi.org/10.1029/2009JB007021

Agius, M. R., & Lebedev, S. (2014). Shear-velocity structure, radial anisotropy and dynamics of the Tibetan crust. *Geophysical Journal International*, *199*(3), 1395–1415. https://doi.org/10.1093/gji/ggu326

An, W., Hu, X., Garzanti, E., Wang, J. G., & Liu, Q. (2021). New precise dating of the India-Asia collision in the Tibetan Himalaya at 61 Ma. *Geophysical Research Letters*, *48*(3), e2020GL090641. https://doi.org/10.1029/2020GL090641

Argand, E. (1924). La tectonique de l'Asie. *Proceedings of the 13th International Geological Congress*.

Arora, B. R., Unsworth, M. J., & Rawat, G. (2007). Deep resistivity structure of the northwest Indian Himalaya and its tectonic implications. *Geophysical Research Letters*, *34*(4), L04307. https://doi.org/10.1029/2006GL029165

Ashish, A., Padhi, A., Rai, S. S., & Gupta, S. (2009). Seismological evidence for shallow crustal melt beneath the Garhwal High Himalaya, India: Implications for the Himalayan channel flow. *Geophysical Journal International*, *177*(3), 1111–1120. https://doi.org/10.1111/j.1365-246X.2009.04112.x

Avouac, J. P., & Tapponnier, P. (1993). Kinematic model of active deformation in central Asia. *Geophysical Research Letters*, *20*(10), 895–898. https://doi.org/10.1029/93GL00128

Bai, D., Unsworth, M. J., Meju, M. A., Ma, X., Teng, J., Kong, X., et al. (2010). Crustal deformation of the eastern Tibetan plateau revealed by magnetotelluric imaging. *Nature Geoscience*, *3*(5), 358–362. https://doi.org/10.1038/ngeo830

Bao, F., Ni, S., Xie, J., Zeng, X., Li, Z., & Li, Z. (2014). Validating accuracy of Rayleigh-wave dispersion extracted from ambient seismic noise via comparison with data from a ground-truth earthquake. *Bulletin of the Seismological Society of America*, *104*(4), 2133–2141. https://doi.org/10.1785/0120130279

Bao, X., Sun, X., Xu, M., Eaton, D. W., Song, X., Wang, L., et al. (2015). Two crustal low-velocity channels beneath SE Tibet revealed by joint inversion of Rayleigh wave dispersion and receiver functions. *Earth and Planetary Science Letters*, *415*, 16–24. https://doi.org/10.1016/j.epsl.2015.01.020

Bard, J. P. (1983). Metamorphism of an obducted island arc: Example of the Kohistan sequence (Pakistan) in the Himalayan collided range. *Earth and Planetary Science Letters*, *65*(1), 133–144. https://doi.org/10.1016/0012-821X(83)90195-4

Bayes, T. (1763). LII. An essay towards solving a problem in the doctrine of chances. By the late Rev. Mr. Bayes, FRS communicated by Mr. Price, in a letter to John Canton, A. M. F. R. S. *Philosophical Transactions of the Royal Society of London*, *53*, 370–418. https://doi.org/10.1098/rstl.1763.0053

Beaumont, C., Jamieson, R. A., Nguyen, M. H., & Medvedev, S. (2004). Crustal channel flows: 1. Numerical models with applications to the tectonics of the Himalayan-Tibetan orogen. *Journal of Geophysical Research: Solid Earth*, *109*(B6), B06406. https://doi.org/10.1029/2003JB002809

Bensen, G. D., Ritzwoller, M. H., Barmin, M. P., Levshin, A. L., Lin, F., Moschetti, M. P., et al. (2007). Processing seismic ambient noise data to obtain reliable broad-band surface wave dispersion measurements. *Geophysical Journal International*, *169*(3), 1239–1260. https://doi.org/10.1111/j.1365-246X.2007.03374.x

Bilham, R., Mencin, D., Bendick, R., & Bürgmann, R. (2017). Implications for elastic energy storage in the Himalaya from the Gorkha 2015 earthquake and other incomplete ruptures of the Main Himalayan Thrust. *Quaternary International*, *462*, 3–21. https://doi.org/10.1016/j.quaint.2016.09.055

Bodin, T., Sambridge, M., Rawlinson, N., & Arroucau, P. (2012). Transdimensional tomography with unknown data noise. *Geophysical Journal International*, *189*(3), 1536–1556. https://doi.org/10.1111/j.1365-246X.2012.05414.x

Bodin, T., Sambridge, M., Tkalčić, H., Arroucau, P., Gallagher, K., & Rawlinson, N. (2012). Transdimensional inversion of receiver functions and surface wave dispersion. *Journal of Geophysical Research: Solid Earth*, *117*(B2), B02301. https://doi.org/10.1029/2011JB008560

Brown, E. T., Bendick, R., Bourles, D. L., Gaur, V., Molnar, P., Raisbeck, G. M., & Yiou, F. (2002). Slip rates of the Karakoram Fault, Ladakh, India, determined using cosmic ray exposure dating of debris flows and moraines. *Journal of Geophysical Research: Solid Earth*, *107*(B9), ESE 7–1–ESE 7–13. https://doi.org/10.1029/2000JB000100

Brown, L. D., Zhao, W., Nelson, K. D., Hauck, M., Alsdorf, D., Ross, A., et al. (1996). Bright spots, structure, and magmatism in southern Tibet from INDEPTH seismic reflection profiling. *Science*, *274*(5293), 1688–1690. https://doi.org/10.1126/science.274.5293.1688

Burchfiel, B. C., & Royden, L. H. (1985). North-south extension within the convergent Himalayan region. *Geology*, *13*(10), 679–682. https://doi.org/10.1130/0091-7613(1985)13<679:NEWTCH>2.0.CO;2

Burtman, V. S., & Molnar, P. H. (1993). *Geological and geophysical evidence for deep subduction of continental crust beneath the Pamir* (Vol. 281). Geological Society of America. https://doi.org/10.1130/SPE281-p1

Caldwell, W. B., Klemperer, S. L., Lawrence, J. F., & Rai, S. S. (2013). Characterizing the Main Himalayan Thrust in the Garhwal Himalaya, India with receiver function CCP stacking. *Earth and Planetary Science Letters*, *367*, 15–27. https://doi.org/10.1016/j.epsl.2013.02.009

Caldwell, W. B., Klemperer, S. L., Rai, S. S., & Lawrence, J. F. (2009). Partial melt in the upper-middle crust of the northwest Himalaya revealed by Rayleigh wave dispersion. *Tectonophysics*, *477*(1–2), 58–65. https://doi.org/10.1016/j.tecto.2009.01.013

Chen, L., Capitanio, F. A., Liu, L., & Gerya, T. V. (2017). Crustal rheology controls on the Tibetan plateau formation during India-Asia convergence. *Nature Communications*, *8*(1), 1–8. https://doi.org/10.1038/ncomms15992

Chen, W. P., Martin, M., Tseng, T. L., Nowack, R. L., Hung, S. H., & Huang, B. S. (2010). Shear-wave birefringence and current configuration of converging lithosphere under Tibet. *Earth and Planetary Science Letters*, *295*(1–2), 297–304. https://doi.org/10.1016/j.epsl.2010.04.017

Christensen, N. I. (1996). Poisson's ratio and crustal seismology. *Journal of Geophysical Research: Solid Earth*, *101*(B2), 3139–3156. https://doi.org/10.1029/95JB03446

Christensen, N. I., & Mooney, W. D. (1995). Seismic velocity structure and composition of the continental crust: A global view. *Journal of Geophysical Research: Solid Earth*, *100*(B6), 9761–9788. https://doi.org/10.1029/95JB00259

Clark, M. K., & Royden, L. H. (2000). Topographic ooze: Building the eastern margin of Tibet by lower crustal flow. *Geology*, *28*(8), 703–706. https://doi.org/10.1130/0091-7613(2000)28<703:TOBTEM>2.0.CO;2

Copley, A., Avouac, J. P., & Royer, J. Y. (2010). India-Asia collision and the Cenozoic slowdown of the Indian plate: Implications for the forces driving plate motions. *Journal of Geophysical Research: Solid Earth*, *115*(B3), B03410. https://doi.org/10.1029/2009JB006634

Corfield, R. I., & Searle, M. P. (2000). Crustal shortening estimates across the north Indian continental margin, Ladakh, NW India. *Geological Society, London, Special Publications*, *170*(1), 395–410. https://doi.org/10.1144/GSL.SP.2000.170.01.21

Dal Zilio, L., Jolivet, R., & van Dinther, Y. (2020). Segmentation of the Main Himalayan Thrust illuminated by Bayesian inference of interseismic coupling. *Geophysical Research Letters*, *47*(4), e2019GL086424. https://doi.org/10.1029/2019GL086424

DeCelles, P. G., Kapp, P., Gehrels, G. E., & Ding, L. (2014). Paleocene-Eocene foreland basin evolution in the Himalaya of southern Tibet and Nepal: Implications for the age of initial India-Asia collision. *Tectonics*, *33*(5), 824–849. https://doi.org/10.1002/2014TC003522

DeCelles, P. G., Robinson, D. M., & Zandt, G. (2002). Implications of shortening in the Himalayan fold-thrust belt for uplift of the Tibetan Plateau. *Tectonics*, *21*(6), 12–1–12–25. https://doi.org/10.1029/2001TC001322

De Sigoyer, J., Guillot, S., & Dick, P. (2004). Exhumation of the ultrahigh-pressure Tso Morari unit in eastern Ladakh (NW Himalaya): A case study. *Tectonics*, *23*(3), TC3003. https://doi.org/10.1029/2002TC001492

Dewey, J. F., & Burke, K. C. (1973). Tibetan, Variscan, and Precambrian basement reactivation: Products of continental collision. *The Journal of Geology*, *81*(6), 683–692. https://doi.org/10.1086/627920

Diaferia, G., & Cammarano, F. (2017). Seismic signature of the continental crust: What thermodynamics says. An example from the Italian peninsula. *Tectonics*, *36*, 3192–3208. https://doi.org/10.1002/2016tc004405

DiPietro, J. A., & Pogue, K. R. (2004). Tectonostratigraphic subdivisions of the Himalaya: A view from the west. *Tectonics*, *23*(5), TC5001. https://doi.org/10.1029/2003TC001554

England, P., & Houseman, G. (1985). Role of lithospheric strength heterogeneities in the tectonics of Tibet and neighboring regions. *Nature*, *315*(6017), 297–301. https://doi.org/10.1038/315297a0

England, P., & Houseman, G. (1986). Finite strain calculations of continental deformation: 2. Comparison with the India-Asia collision zone. *Journal of Geophysical Research: Solid Earth*, *91*(B3), 3664–3676. https://doi.org/10.1029/JB091iB03p03664

England, P., & McKenzie, D. (1982). A thin viscous sheet model for continental deformation. *Geophysical Journal International*, *70*(2), 295–321. https://doi.org/10.1111/j.1365-246X.1982.tb04969.x

England, P., & Molnar, P. (2005). Late Quaternary to decadal velocity fields in Asia. *Journal of Geophysical Research: Solid Earth*, *110*(B12), B12401. https://doi.org/10.1029/2004JB003541

Eugster, P., Thiede, R. C., Scherler, D., Stübner, K., Sobel, E. R., & Strecker, M. R. (2018). Segmentation of the Main Himalayan thrust revealed by low-temperature thermochronometry in the western Indian Himalaya. *Tectonics*, *37*(8), 2710–2726. https://doi.org/10.1029/2017TC004752

Feld, C., Haberland, C., Schurr, B., Sippl, C., Wetzel, H. U., Roessner, S., et al. (2015). Seismotectonic study of the Fergana Region (Southern Kyrgyzstan): Distribution and kinematics of local seismicity. *Earth Planets and Space*, *67*(1), 1–13. https://doi.org/10.1186/s40623-015-0195-1

Galvé, A., Jiang, M., Hirn, A., Sapin, M., Laigle, M., De Voogd, B., et al. (2006). Explosion seismic *P* and *S* velocity and attenuation constraints on the lower crust of the North-Central Tibetan Plateau, and comparison with the Tethyan Himalayas: Implications on composition, mineralogy, temperature, and tectonic evolution. *Tectonophysics*, *412*(3–4), 141–157. https://doi.org/10.1016/j.tecto.2005.09.010

Gan, W., Zhang, P., Shen, Z. K., Niu, Z., Wang, M., Wan, Y., et al. (2007). Present-day crustal motion within the Tibetan Plateau inferred from GPS measurements. *Journal of Geophysical Research: Solid Earth*, *112*(B8), B08416. https://doi.org/10.1029/2005JB004120

Geyer, C., & Møller, J. (1994). Simulation procedures and likelihood inference for spatial point processes. *Scandinavian Journal of Statistics*, *21*(4), 359–373. http://www.jstor.org/stable/4616323

Gilligan, A., & Priestley, K. F. (2018). Lateral variations in the crustal structure of the Indo-Eurasian collision zone. *Geophysical Journal International*, *214*(2), 975–989. https://doi.org/10.1093/gji/ggy172

Gilligan, A., Priestley, K. F., Roecker, S. W., Levin, V., & Rai, S. S. (2015). The crustal structure of the western Himalayas and Tibet. *Journal of Geophysical Research: Solid Earth*, *120*(5), 3946–3964. https://doi.org/10.1002/2015JB011891

Green, P. J. (1995). Reversible jump MCMC computation and Bayesian model determination. *Biometrika*, *82*, 711–732. https://doi.org/10.1093/biomet/82.4.711

Griffin, J. D., Nowack, R. L., Chen, W. P., & Tseng, T. L. (2011). Velocity structure of the Tibetan lithosphere: Constraints from *P* wave travel-times of regional earthquakes. *Bulletin of the Seismological Society of America*, *101*(4), 1938–1947. https://doi.org/10.1785/0120100229

Grujic, D., Casey, M., Davidson, C., Hollister, L. S., Kündig, R., Pavlis, T., & Schmid, S. (1996). Ductile extrusion of the Higher Himalayan crystalline in Bhutan: Evidence from quartz microfabrics. *Tectonophysics*, *260*(1–3), 21–43. https://doi.org/10.1016/0040-1951(96)00074-1

Grujic, D., Hollister, L. S., & Parrish, R. R. (2002). Himalayan metamorphic sequence as an orogenic channel: Insight from Bhutan. *Earth and Planetary Science Letters*, *198*(1–2), 177–191. https://doi.org/10.1016/S0012-821X(02)00482-X

Guillot, S., Goussin, F., Airaghi, L., Replumaz, A., De Sigoyer, J., & Cordier, C. (2019). How and when did the Tibetan Plateau grow? *Russian Geology and Geophysics*, *60*(9), 957–977. https://doi.org/10.15372/RGG2019126

Guillot, S., Replumaz, A., Hattori, K. H., & Strzerzynski, P. (2007). Initial geometry of western Himalaya and ultrahigh-pressure metamorphic evolution. *Journal of Asian Earth Sciences*, *30*(3–4), 557–564. https://doi.org/10.1016/j.jseaes.2007.01.004

Hable, S., Sigloch, K., Stutzmann, E., Kiselev, S., & Barruol, G. (2019). Tomography of crust and lithosphere in the western Indian Ocean from noise cross-correlations of land and ocean bottom seismometers. *Geophysical Journal International*, *219*(2), 924–944. https://doi.org/10.1093/gji/ggz333

Hacker, B. R., Luffi, P., Lutkov, V., Minaev, V., Ratschbacher, L., Plank, T., et al. (2005). Near-ultrahigh pressure processing of continental crust: Miocene crustal xenoliths from the Pamir. *Journal of Petrology*, *46*(8), 1661–1687. https://doi.org/10.1093/petrology/egi030

Hacker, B. R., Ratschbacher, L., Rutte, D., Stearns, M. A., Malz, N., Stübner, K., et al. (2017). Building the Pamir-Tibet Plateau—Crustal stacking, extensional collapse, and lateral extrusion in the Pamir: 3. Thermobarometry and petrochronology of deep Asian crust. *Tectonics*, *36*(9), 1743–1766. https://doi.org/10.1002/2017TC004488

Hacker, B. R., Ritzwoller, M. H., & Xie, J. (2014). Partially melted, mica-bearing crust in Central Tibet. *Tectonics*, *33*(7), 1408–1424. https://doi.org/10.1002/2014TC003545

Harrison, T. M. (2006). Did the Himalayan Crystallines extrude partially molten from beneath the Tibetan Plateau? *Geological Society, London, Special Publications*, *268*(1), 237–254. https://doi.org/10.1144/GSL.SP.2006.268.01.11

Hawkins, R., Brodie, R. C., & Sambridge, M. (2018). Trans-dimensional Bayesian inversion of airborne electromagnetic data for 2-D conductivity profiles. *Exploration Geophysics*, *49*(2), 134–147. https://doi.org/10.1071/EG16139

Hawkins, R., & Sambridge, M. (2015). Geophysical imaging using trans-dimensional trees. *Geophysical Journal International*, *203*(2), 972–1000. https://doi.org/10.1093/gji/ggv326

Hazarika, D., Wadhawan, M., Paul, A., Kumar, N., & Borah, K. (2017). Geometry of the Main Himalayan Thrust and Moho beneath Satluj valley, northwest Himalaya: Constraints from receiver function analysis. *Journal of Geophysical Research: Solid Earth*, *122*(4), 2929–2945. https://doi.org/10.1002/2016JB013783

He, P., Lei, J., Yuan, X., Xu, X., Xu, Q., Liu, Z., et al. (2018). Lateral Moho variations and the geometry of the Main Himalayan thrust beneath the Nepal Himalayan orogen revealed by teleseismic receiver functions. *Geophysical Journal International*, *214*(2), 1004–1017. https://doi.org/10.1093/gji/ggy192

Heim, A., & Gansser, A. (1939). *Central Himalaya: Geological observations of Swiss expedition 1936* (Vol. 246). Hindustan Publishing Corporation. https://doi.org/10.1111/j.2044-8295.1939.tb00916.x

Hetényi, G., Cattin, R., Berthet, T., Le Moigne, N., Chophel, J., Lechmann, S., et al. (2016). Segmentation of the Himalayas as revealed by arc-parallel gravity anomalies. *Scientific Reports*, *6*(1), 1–10. https://doi.org/10.1038/srep33866

Hetényi, G., Vergne, J., Bollinger, L., & Cattin, R. (2011). Discontinuous low-velocity zones in southern Tibet question the viability of the channel flow model. *Geological Society, London, Special Publications*, *353*(1), 99–108. https://doi.org/10.1144/SP353.6

Hintersberger, E., Thiede, R. C., & Strecker, M. R. (2011). The role of extension during brittle deformation within the NW Indian Himalaya. *Tectonics*, *30*(3), TC3012. https://doi.org/10.1029/2010TC002822

Hodges, K. V. (2006). A synthesis of the channel flow-extrusion hypothesis as developed for the Himalayan-Tibetan orogenic system. *Geological Society, London, Special Publications*, *268*(1), 71–90. https://doi.org/10.1144/GSL.SP.2006.268.01.04

Huang, G. C. D., Roecker, S. W., & Levin, V. (2011). Lower-crustal earthquakes in the West Kunlun range. *Geophysical Research Letters*, *38*(1), L01314. https://doi.org/10.1029/2010GL045893

Huang, G. C. D., Wu, F. T., Roecker, S. W., & Sheehan, A. F. (2009). Lithospheric structure of the central Himalaya from 3-D tomographic imaging. *Tectonophysics*, *475*(3–4), 524–543. https://doi.org/10.1016/j.tecto.2009.06.023

Jade, S., Bhatt, B. C., Yang, Z., Bendick, R., Gaur, V. K., Molnar, P., et al. (2004). GPS measurements from the Ladakh Himalaya, India: Preliminary tests of plate-like or continuous deformation in Tibet. *The Geological Society of America Bulletin*, *116*(11–12), 1385–1391. https://doi.org/10.1130/B25357.1

Jagoutz, O., & Kelemen, P. B. (2015). Role of arc processes in the formation of continental crust. *Annual Review of Earth and Planetary Sciences*, *43*, 363–404. https://doi.org/10.1146/annurev-earth-040809-152345

Jia, C. (1997). *Tectonic characteristics and petroleum, Tarim basin*. Petroleum Industry Press.

Johnson, M. R. W. (2002). Shortening budgets and the role of continental subduction during the India-Asia collision. *Earth-Science Reviews*, *59*(1–4), 101–123. https://doi.org/10.1016/S0012-8252(02)00071-5

Jones, R. R., Holdsworth, R. E., Hand, M., & Goscombe, B. (2006). Ductile extrusion in continental collision zones: Ambiguities in the definition of channel flow and its identification in ancient orogens. *Geological Society, London, Special Publications*, *268*(1), 201–219. https://doi.org/10.1144/GSL.SP.2006.268.01.09

Julia, J., Jagadeesh, S., Rai, S. S., & Owens, T. J. (2009). Deep crustal structure of the Indian shield from joint inversion of *P* wave receiver functions and Rayleigh wave group velocities: Implications for Precambrian crustal evolution. *Journal of Geophysical Research: Solid Earth*, *114*(B10), B10313. https://doi.org/10.1029/2008JB006261

Kao, H., Gao, R., Rau, R. J., Shi, D., Chen, R. Y., Guan, Y., & Wu, F. T. (2001). Seismic image of the Tarim basin and its collision with Tibet. *Geology*, *29*(7), 575–578. https://doi.org/10.1130/0091-7613(2001)029<0575:SIOTTB>2.0.CO;2

Kapp, P., & DeCelles, P. G. (2019). Mesozoic-Cenozoic geological evolution of the Himalayan-Tibetan orogen and working tectonic hypotheses. *American Journal of Science*, *319*(3), 159–254. https://doi.org/10.2475/03.2019.01

Kelly, S., & Beaumont, C. (2021). Balanced cross-sections and numerical modeling of the lithospheric-scale evolution of the Hindu Kush and Pamir. *Journal of Geophysical Research: Solid Earth*, *126*(3), e2020JB020678. https://doi.org/10.1029/2020JB020678

Kern, H., Popp, T., Gorbatsevich, F., Zharikov, A., Lobanov, K. V., & Smirnov, Y. P. (2001). Pressure and temperature dependence of Vp and Vs in rocks from the superdeep well and from surface analogs at Kola and the nature of velocity anisotropy. *Tectonophysics*, *338*(2), 113–134. https://doi.org/10.1016/S0040-1951(01)00128-7

Khan, N. G., Bai, L., Zhao, J., Li, G., Rahman, M. M., Cheng, C., & Yang, J. (2017). Crustal structure beneath Tien Shan orogenic belt and its adjacent regions from multi-scale seismic data. *Science China Earth Sciences*, *60*(10), 1769–1782. https://doi.org/10.1007/s11430-017-9068-0

Klemperer, S. L. (2006). Crustal flow in Tibet: Geophysical evidence for the physical state of Tibetan lithosphere, and inferred patterns of active flow. *Geological Society, London, Special Publications*, *268*(1), 39–70. https://doi.org/10.1144/GSL.SP.2006.268.01.03

Klemperer, S. L., Kennedy, B. M., Sastry, S. R., Makovsky, Y., Harinarayana, T., & Leech, M. L. (2013). Mantle fluids in the Karakoram fault: Helium isotope evidence. *Earth and Planetary Science Letters*, *366*, 59–70. https://doi.org/10.1016/j.epsl.2013.01.013

Kosarev, G., Kind, R., Sobolev, S. V., Yuan, X., Hanka, W., & Oreshin, S. (1999). Seismic evidence for a detached Indian lithospheric mantle beneath Tibet. *Science*, *283*(5406), 1306–1309. https://doi.org/10.1126/science.283.5406.1306

Kufner, S. K., Schurr, B., Haberland, C., Zhang, Y., Saul, J., Ischuk, A., & Oimahmadov, I. (2017). Zooming into the Hindu Kush slab break-off: A rare glimpse on the terminal stage of subduction. *Earth and Planetary Science Letters*, *461*, 127–140. https://doi.org/10.1016/j.epsl.2016.12.043

Kufner, S. K., Schurr, B., Sippl, C., Yuan, X., Ratschbacher, L., Ischuk, A., et al. (2016). Deep India meets deep Asia: Lithospheric indentation, delamination and break-off under Pamir and Hindu Kush (central Asia). *Earth and Planetary Science Letters*, *435*, 171–184. https://doi.org/10.1016/j.epsl.2015.11.046

Kumar, N., Aoudia, A., Guidarelli, M., Babu, V. G., Hazarika, D., & Yadav, D. K. (2019). Delineation of lithosphere structure and characterization of the Moho geometry under the Himalaya-Karakoram-Tibet collision zone using surface-wave tomography. *Geological Society, London, Special Publications*, *481*(1), 19–40. https://doi.org/10.1144/SP481-2017-172

Law, R. D., Searle, M. P., & Simpson, R. L. (2004). Strain, deformation temperatures, and vorticity of flow at the top of the Greater Himalayan Slab, Everest Massif, Tibet. *Journal of the Geological Society*, *161*(2), 305–320. https://doi.org/10.1144/0016-764903-047

Lebedev, S., Adam, J. M. C., & Meier, T. (2013). Mapping the Moho with seismic surface waves: A review, resolution analysis, and recommended inversion strategies. *Tectonophysics*, *609*, 377–394. https://doi.org/10.1016/j.tecto.2012.12.030

Leech, M. L. (2008). Does the Karakoram fault interrupt mid-crustal channel flow in the western Himalaya? *Earth and Planetary Science Letters*, *276*(3–4), 314–322. https://doi.org/10.1016/j.epsl.2008.10.006

Leech, M. L., Singh, S., Jain, A. K., Klemperer, S. L., & Manickavasagam, R. M. (2005). The onset of India-Asia continental collision: Early, steep subduction required by the timing of UHP metamorphism in the western Himalaya. *Earth and Planetary Science Letters*, *234*(1–2), 83–97. https://doi.org/10.1016/j.epsl.2005.02.038

Leier, A. L., Kapp, P., Gehrels, G. E., & DeCelles, P. G. (2007). Detrital zircon geochronology of Carboniferous-Cretaceous strata in the Lhasa terrane, southern Tibet. *Basin Research*, *19*(3), 361–378. https://doi.org/10.1111/j.1365-2117.2007.00330.x

Levshin, A. L., & Ritzwoller, M. H. (2001). Automated detection, extraction, and measurement of regional surface waves. In *Monitoring the comprehensive nuclear-test-ban treaty: Surface waves* (pp. 1531–1545). Birkhäuser. https://doi.org/10.1007/978-3-0348-8264-4_11

Li, C., Van der Hilst, R. D., Meltzer, A. S., & Engdahl, E. R. (2008). Subduction of the Indian lithosphere beneath the Tibetan Plateau and Burma. *Earth and Planetary Science Letters*, *274*(1–2), 157–168. https://doi.org/10.1016/j.epsl.2008.07.016

Li, J., & Song, X. (2018). Tearing of Indian mantle lithosphere from high-resolution seismic images and its implications for lithosphere coupling in southern Tibet. *Proceedings of the National Academy of Sciences*, *115*(33), 8296–8300. https://doi.org/10.1073/pnas.1717258115

Li, L., Murphy, M. A., & Gao, R. (2020). Subduction of the Indian plate and the nature of the crust beneath western Tibet: Insights from seismic imaging. *Journal of Geophysical Research: Solid Earth*, *125*(8), e2020JB019684. https://doi.org/10.1029/2020JB019684

Li, W., Chen, Y., Tan, P., & Yuan, X. (2020). Geodynamic processes of the continental deep subduction: Constraints from the fine crustal structure beneath the Pamir plateau. *Science China Earth Sciences*, *63*(5), 649–661. https://doi.org/10.1007/s11430-019-9587-3

Li, W., Chen, Y., Yuan, X., Schurr, B., Mechie, J., Oimahmadov, I., & Fu, B. (2018). Continental lithospheric subduction and intermediate-depth seismicity: Constraints from *S* wave velocity structures in the Pamir and Hindu Kush. *Earth and Planetary Science Letters*, *482*, 478–489. https://doi.org/10.1016/j.epsl.2017.11.031

Liang, X., Zhou, S., Chen, Y. J., Jin, G., Xiao, L., Liu, P., et al. (2008). Earthquake distribution in southern Tibet and its tectonic implications. *Journal of Geophysical Research: Solid Earth*, *113*(B12), B12409. https://doi.org/10.1029/2007JB005101

Litvinovsky, B. A., Steele, I. M., & Wickham, S. M. (2000). Silicic magma formation in overthickened crust: Melting of charnockite and leucogranite at 15, 20, and 25 kbar. *Journal of Petrology*, *41*(5), 717–737. https://doi.org/10.1093/petrology/41.5.717

Loveless, J. P., & Meade, B. J. (2011). Partitioning of localized and diffuse deformation in the Tibetan Plateau from joint inversions of geologic and geodetic observations. *Earth and Planetary Science Letters*, *303*(1–2), 11–24. https://doi.org/10.1016/j.epsl.2010.12.014

Maceira, M., & Ammon, C. J. (2009). Joint inversion of surface wave velocity and gravity observations and its application to central Asian basins shear velocity structure. *Journal of Geophysical Research: Solid Earth*, *114*(B2), B02314. https://doi.org/10.1029/2007JB005157

Mahesh, P., Rai, S. S., Sivaram, K., Paul, A., Gupta, S., Sarma, R., & Gaur, V. K. (2013). One-dimensional reference velocity model and precise locations of earthquake hypocenters in the Kumaon-Garhwal Himalaya. *Bulletin of the Seismological Society of America*, *103*(1), 328–339. https://doi.org/10.1785/0120110328

Makovsky, Y., & Klemperer, S. L. (1999). Measuring the seismic properties of Tibetan bright spots: Evidence for free aqueous fluids in the Tibetan middle crust. *Journal of Geophysical Research: Solid Earth*, *104*(B5), 10795–10825. https://doi.org/10.1029/1998JB900074

Malinverno, A., & Briggs, V. A. (2004). Expanded uncertainty quantification in inverse problems: Hierarchical Bayes and empirical Bayes. *Geophysics*, *69*(4), 1005–1016. https://doi.org/10.1190/1.1778243

McKenzie, D., & Sclater, J. G. (1971). The evolution of the Indian Ocean since the Late Cretaceous. *Geophysical Journal International*, *24*(5), 437–528. https://doi.org/10.1111/j.1365-246X.1971.tb02190.x

Mechie, J., Yuan, X., Schurr, B., Schneider, F., Sippl, C., Ratschbacher, L., et al. (2012). Crustal and uppermost mantle velocity structure along a profile across the Pamir and southern Tien Shan as derived from project TIPAGE wide-angle seismic data. *Geophysical Journal International*, *188*(2), 385–407. https://doi.org/10.1111/j.1365-246X.2011.05278.x

Meng, J., Gilder, S. A., Li, Y., Wang, C., & Liu, T. (2020). Expanse of Greater India in the Late Cretaceous. *Earth and Planetary Science Letters*, *542*, 116330. https://doi.org/10.1016/j.epsl.2020.116330

Mir, R. R., Parvez, I. A., Gaur, V. K., Chandra, R., & Romshoo, S. A. (2017). Crustal structure beneath the Kashmir basin adjoining the western Himalayan syntaxis. *Bulletin of the Seismological Society of America*, *107*(5), 2443–2458. https://doi.org/10.1785/0120150334

Molnar, P., England, P., & Martinod, J. (1993). Mantle dynamics, uplift of the Tibetan Plateau, and the Indian monsoon. *Reviews of Geophysics*, *31*(4), 357–396. https://doi.org/10.1029/93RG02030

Molnar, P., & Tapponnier, P. (1975). Cenozoic tectonics of Asia: Effects of a continental collision. *Science*, *189*(4201), 419–426. https://doi.org/10.1126/science.189.4201.419

Monsalve, G., Sheehan, A., Rowe, C., & Rajaure, S. (2008). Seismic structure of the crust and the upper mantle beneath the Himalayas: Evidence for eclogitization of lower crustal rocks in the Indian Plate. *Journal of Geophysical Research: Solid Earth*, *113*(B8), B08315. https://doi.org/10.1029/2007JB005424

Murodov, D., Zhao, J., Xu, Q., Liu, H., & Pei, S. (2018). Complex N-S variations in Moho depth and Vp/Vs ratio beneath the western Tibetan Plateau as revealed by receiver function analysis. *Geophysical Journal International*, *214*(2), 895–906. https://doi.org/10.1093/gji/ggy170

Murphy, M. A., & Copeland, P. (2005). Transtensional deformation in the central Himalaya and its role in accommodating growth of the Himalayan orogen. *Tectonics*, *24*(4), TC4012. https://doi.org/10.1029/2004TC001659

Nábělek, J., Hetényi, G., Vergne, J., Sapkota, S., Kafle, B., Jiang, M., et al. (2009). Underplating in the Himalaya-Tibet collision zone revealed by the Hi-CLIMB experiment. *Science*, *325*(5946), 1371–1374. https://doi.org/10.1126/science.1167719

Nelson, K. D., Zhao, W., Brown, L. D., Kuo, J., Che, J., Liu, X., et al. (1996). Partially molten middle crust beneath southern Tibet: Synthesis of project INDEPTH results. *Science*, *274*(5293), 1684–1688. https://doi.org/10.1126/science.274.5293.1684

Nowack, R. L., Chen, W. P., & Tseng, T. L. (2010). Application of Gaussian-beam migration to multiscale imaging of the lithosphere beneath the Hi-CLIMB array in Tibet. *Bulletin of the Seismological Society of America*, *100*(4), 1743–1754. https://doi.org/10.1785/0120090207

Owens, T. J., & Zandt, G. (1997). Implications of crustal property variations for models of Tibetan plateau evolution. *Nature*, *387*(6628), 37–43. https://doi.org/10.1038/387037a0

Pasyanos, M. E. (2005). A variable resolution surface wave dispersion study of Eurasia, North Africa, and surrounding regions. *Journal of Geophysical Research: Solid Earth*, *110*(B12), B12301. https://doi.org/10.1029/2005JB003749

Pegler, G., & Das, S. (1998). An enhanced image of the Pamir-Hindu Kush seismic zone from relocated earthquake hypocentres. *Geophysical Journal International*, *134*(2), 573–595. https://doi.org/10.1046/j.1365-246x.1998.00582.x

Pei, S., Sun, Y., & Toksöz, M. N. (2011). Tomographic Pn and Sn velocity beneath the continental collision zone from Alps to Himalaya. *Journal of Geophysical Research: Solid Earth*, *116*(B10), B10311. https://doi.org/10.1029/2010JB007845

Pilia, S., Jackson, J. A., Hawkins, R., Kaviani, A., & Ali, M. Y. (2020). The southern Zagros collisional orogen: New insights from transdimensional trees inversion of seismic noise. *Geophysical Research Letters*, *47*(4), e2019GL086258. https://doi.org/10.1029/2019GL086258

Powell, C. M., & Conaghan, P. J. (1973). Plate tectonics and the Himalayas. *Earth and Planetary Science Letters*, *20*(1), 1–12. https://doi.org/10.1016/0012-821X(73)90134-9

Priestley, K., Ho, T., & Mitra, S. (2019). The crustal structure of the Himalaya: A synthesis. *Geological Society, London, Special Publications*, *483*(1), 483–516. https://doi.org/10.1144/SP483-2018-127

Priestley, K., Jackson, J., & McKenzie, D. (2008). Lithospheric structure and deep earthquakes beneath India, the Himalaya and southern Tibet. *Geophysical Journal International*, *172*(1), 345–362. https://doi.org/10.1111/j.1365-246X.2007.03636.x

Rai, S. S., Padhi, A., & Sarma, P. R. (2009). High crustal seismic attenuation in Ladakh-Karakoram. *Bulletin of the Seismological Society of America*, *99*(1), 407–415. https://doi.org/10.1785/0120070261

Rai, S. S., Priestley, K., Gaur, V. K., Mitra, S., Singh, M. P., & Searle, M. (2006). Configuration of the Indian Moho beneath the NW Himalaya and Ladakh. *Geophysical Research Letters*, *33*(15), L15308. https://doi.org/10.1029/2006GL026076

Rawlinson, N., & Sambridge, M. (2005). The fast marching method: An effective tool for tomographic imaging and tracking multiple phases in complex layered media. *Exploration Geophysics*, *36*(4), 341–350. https://doi.org/10.1071/EG05341

Rawlinson, N., & Spakman, W. (2016). On the use of sensitivity tests in seismic tomography. *Geophysical Journal International*, *205*(2), 1221–1243. https://doi.org/10.1093/gji/ggw084

Razi, A. S., Levin, V., Roecker, S. W., & Huang, G. C. D. (2014). Crustal and uppermost mantle structure beneath western Tibet using seismic travel-time tomography. *Geochemistry, Geophysics, Geosystems*, *15*(2), 434–452. https://doi.org/10.1002/2013GC005143

Reguzzoni, M., Sampietro, D., & Sansò, F. (2013). Global Moho from the combination of the CRUST2.0 model and GOCE data. *Geophysical Journal International*, *195*(1), 222–237. https://doi.org/10.1093/gji/ggt247

Rippe, D., & Unsworth, M. (2010). Quantifying crustal flow in Tibet with magnetotelluric data. *Physics of the Earth and Planetary Interiors*, *179*(3–4), 107–121. https://doi.org/10.1016/j.pepi.2010.01.009

Ritzwoller, M. H., Lin, F. C., & Shen, W. (2011). Ambient noise tomography with a large seismic array. *Comptes Rendus Geoscience*, *343*(8–9), 558–570. https://doi.org/10.1016/j.crte.2011.03.007

Rosalia, S., Cummins, P., Widiyantoro, S., Yudistira, T., Nugraha, A. D., & Hawkins, R. (2020). Group velocity maps using subspace and transdimensional inversions: Ambient noise tomography in the western part of Java, Indonesia. *Geophysical Journal International*, *220*(2), 1260–1274. https://doi.org/10.1093/gji/ggz498

Royden, L. H., Burchfiel, B. C., & van der Hilst, R. D. (2008). The geological evolution of the Tibetan Plateau. *Science*, *321*(5892), 1054–1058. https://doi.org/10.1126/science.1155371

Rudnick, R. L., & Fountain, D. M. (1995). Nature and composition of the continental crust: A lower crustal perspective. *Reviews of Geophysics*, *33*(3), 267–309. https://doi.org/10.1029/95RG01302

Rudnick, R. L., & Gao, S. (2003). *Treatise on geochemistry* (Vol. 3). Composition of the Continental Crust.

Rutte, D., Ratschbacher, L., Khan, J., Stübner, K., Hacker, B. R., Stearns, M. A., et al. (2017). Building the Pamir-Tibetan Plateau-Crustal stacking, extensional collapse, and lateral extrusion in the Central Pamir: 2. Timing and rates. *Tectonics*, *36*(3), 385–419. https://doi.org/10.1002/2016TC004293

Saha, G. K., Prakasam, K. S., & Rai, S. S. (2020). Diversity in the peninsular Indian lithosphere revealed from ambient noise and earthquake tomography. *Physics of the Earth and Planetary Interiors*, *306*, 106523. https://doi.org/10.1016/j.pepi.2020.106523

Saito, M. A. S. A. N. O. R. I. (1988). DISPER80: A subroutine package for the calculation of seismic normal-mode solutions. *Seismological Algorithms: Computational Methods and Computer Programs* (pp. 293–319). Academic Press.

Sapin, M., & Hirn, A. (1997). Seismic structure and evidence for eclogitization during the Himalayan convergence. *Tectonophysics*, *273*(1–2), 1–16. https://doi.org/10.1016/S0040-1951(96)00285-5

Sass, P., Ritter, O., Ratschbacher, L., Tympel, J., Matiukov, V. E., Rybin, A. K., & Batalev, V. Y. (2014). Resistivity structure underneath the Pamir and southern Tian Shan. *Geophysical Journal International*, *198*(1), 564–579. https://doi.org/10.1093/gji/ggu146

Schimmel, M. (1999). Phase cross-correlations: Design, comparisons, and applications. *Bulletin of the Seismological Society of America*, *89*(5), 1366–1378. https://doi.org/10.1785/bssa0890051366

Schimmel, M., & Gallart, J. (2007). Frequency-dependent phase coherence for noise suppression in seismic array data. *Journal of Geophysical Research: Solid Earth*, *112*(B4), B04303. https://doi.org/10.1029/2006JB004680

Schimmel, M., Stutzmann, E., & Gallart, J. (2011). Using instantaneous phase coherence for signal extraction from ambient noise data at a local to a global scale. *Geophysical Journal International*, *184*(1), 494–506. https://doi.org/10.1111/j.1365-246X.2010.04861.x

Schneider, F. M., Yuan, X., Schurr, B., Mechie, J., Sippl, C., Kufner, S. K., et al. (2019). The crust in the Pamir: Insights from receiver functions. *Journal of Geophysical Research: Solid Earth*, *124*(8), 9313–9331. https://doi.org/10.1029/2019JB017765

Schulte-Pelkum, V., Mahan, K. H., Shen, W., & Stachnik, J. C. (2017). The distribution and composition of high-velocity lower crust across the continental US: Comparison of seismic and xenolith data and implications for lithospheric dynamics and history. *Tectonics*, *36*(8), 1455–1496. https://doi.org/10.1002/2017TC004480

Schulte-Pelkum, V., Monsalve, G., Sheehan, A., Pandey, M. R., Sapkota, S., Bilham, R., & Wu, F. (2005). Imaging the Indian subcontinent beneath the Himalaya. *Nature*, *435*(7046), 1222–1225. https://doi.org/10.1038/nature03678

Schulte-Pelkum, V., Monsalve, G., Sheehan, A. F., Shearer, P., Wu, F., & Rajaure, S. (2019). Mantle earthquakes in the Himalayan collision zone. *Geology*, *47*(9), 815–819. https://doi.org/10.1130/G46378.1

Schurr, B., Ratschbacher, L., Sippl, C., Gloaguen, R., Yuan, X., & Mechie, J. (2014). Seismotectonics of the Pamir. *Tectonics*, *33*(8), 1501–1518. https://doi.org/10.1002/2014TC003576

Schwab, M., Ratschbacher, L., Siebel, W., McWilliams, M., Minaev, V., Lutkov, V., et al. (2004). Assembly of the Pamirs: Age and origin of magmatic belts from the southern Tien Shan to the southern Pamirs and their relation to Tibet. *Tectonics*, *23*(4), TC4002. https://doi.org/10.1029/2003TC001583

Searle, M. P., Elliott, J. R., Phillips, R. J., & Chung, S. L. (2011). Crustal-lithospheric structure and continental extrusion of Tibet. *Journal of the Geological Society*, *168*(3), 633–672. https://doi.org/10.1144/0016-76492010-139

Searle, M. P., & Hacker, B. R. (2019). Structural and metamorphic evolution of the Karakoram and Pamir following India-Kohistan-Asia collision. *Geological Society, London, Special Publications*, *483*(1), 555–582. https://doi.org/10.1144/SP483.6

Searle, M. P., Parrish, R. R., Thow, A. V., Noble, S. R., Phillips, R. J., & Waters, D. J. (2010). Anatomy, age and evolution of a collisional mountain belt: The Baltoro granite batholith and Karakoram Metamorphic Complex, Pakistani Karakoram. *Journal of the Geological Society*, *167*(1), 183–202. https://doi.org/10.1144/0016-76492009-043

Seeber, L., Armbruster, J. G., & Quittmeyer, R. C. (1981). Seismicity and continental subduction in the Himalayan arc. *Zagros Hindu Kush Himalaya Geodynamic Evolution*, *3*, 215–242. https://doi.org/10.1029/GD003p0215

Sengör, A. C., & Natal'In, B. A. (1996). Turkic-type orogeny and its role in the making of the continental crust. *Annual Review of Earth and Planetary Sciences*, *24*(1), 263–337. https://doi.org/10.1146/annurev.earth.24.1.263

Shapiro, N. M., & Campillo, M. (2004). Emergence of broadband Rayleigh waves from correlations of the ambient seismic noise. *Geophysical Research Letters*, *31*(7), L07614. https://doi.org/10.1029/2004GL019491

Shapiro, N. M., Campillo, M., Stehly, L., & Ritzwoller, M. H. (2005). High-resolution surface-wave tomography from ambient seismic noise. *Science*, *307*(5715), 1615–1618. https://doi.org/10.1126/science.1108339

Shapiro, N. M., Ritzwoller, M. H., Molnar, P., & Levin, V. (2004). Thinning and flow of Tibetan crust constrained by seismic anisotropy. *Science*, *305*(5681), 233–236. https://doi.org/10.1126/science.1098276

Sharma, S., Mitra, S., Sharma, S., Priestley, K., Wanchoo, S. K., Powali, D., & Ali, L. (2020). A report on broadband seismological experiment in the Jammu and Kashmir Himalaya (JAKSNET). *Seismological Research Letters*, *91*(3), 1915–1926. https://doi.org/10.1785/0220190389

Shen, W., Ritzwoller, M. H., Kang, D., Kim, Y., Lin, F. C., Ning, J., et al. (2016). A seismic reference model for the crust and uppermost mantle beneath China from surface wave dispersion. *Geophysical Journal International*, *206*(2), 954–979. https://doi.org/10.1093/gji/ggw175

Shi, D., Wu, Z., Klemperer, S. L., Zhao, W., Xue, G., & Su, H. (2015). Receiver function imaging of crustal suture, steep subduction, and mantle wedge in the eastern India-Tibet continental collision zone. *Earth and Planetary Science Letters*, *414*, 6–15. https://doi.org/10.1016/j.epsl.2014.12.055

Shi, F., Wang, Y., Yu, T., Zhu, L., Zhang, J., Wen, J., et al. (2018). Lower-crustal earthquakes in southern Tibet are linked to eclogitization of dry metastable granulite. *Nature Communications*, *9*(1), 1–13. https://doi.org/10.1038/s41467-018-05964-1

Sippl, C., Schurr, B., Yuan, X., Mechie, J., Schneider, F. M., Gadoev, M., et al. (2013). Geometry of the Pamir-Hindu Kush intermediate-depth earthquake zone from local seismic data. *Journal of Geophysical Research: Solid Earth*, *118*(4), 1438–1457. https://doi.org/10.1002/jgrb.50128

Stevens, V. L., & Avouac, J. P. (2015). Interseismic coupling on the main Himalayan thrust. *Geophysical Research Letters*, *42*(14), 5828–5837. https://doi.org/10.1002/2015GL064845

Styron, R. H., Taylor, M. H., & Murphy, M. A. (2011). Oblique convergence, arc-parallel extension, and the role of strike-slip faulting in the High Himalaya. *Geosphere*, *7*(2), 582–596. https://doi.org/10.1130/GES00606.1

Tahirkheli, R. K. (1979). Geology of Kohistan and adjoining Eurasian and Indo-Pakistan continents, Pakistan. *Geological Bulletin University of Peshawar*, *11*(1), 1–30.

Takei, Y. (2000). Acoustic properties of partially molten media studied on a simple binary system with a controllable dihedral angle. *Journal of Geophysical Research*, *105*(B7), 16665–16682. https://doi.org/10.1029/2000JB900124

Tapponnier, P., Zhiqin, X., Roger, F., Meyer, B., Arnaud, N., Wittlinger, G., & Jingsui, Y. (2001). Oblique stepwise rise and growth of the Tibet Plateau. *Science*, *294*(5547), 1671–1677. https://doi.org/10.1126/science.105978

Thatcher, W. (2007). Microplate model for the present-day deformation of Tibet. *Journal of Geophysical Research: Solid Earth*, *112*(B1), B01401. https://doi.org/10.1029/2005JB004244

Tseng, T. L., Chen, W. P., & Nowack, R. L. (2009). Northward thinning of Tibetan crust revealed by virtual seismic profiles. *Geophysical Research Letters*, *36*(24), L24304. https://doi.org/10.1029/2009GL040457

Unsworth, M. J., Jones, A. G., Wei, W., Marquis, G., Gokarn, S. G., & Spratt, J. E. (2005). Crustal rheology of the Himalaya and southern Tibet inferred from magnetotelluric data. *Nature*, *438*(7064), 78–81. https://doi.org/10.1038/nature04154

Van Hinsbergen, D. J. J., Lippert, P. C., Dupont-Nivet, G., McQuarrie, N., Doubrovine, P. V., Spakman, W., & Torsvik, T. H. (2012). Greater India Basin hypothesis and a two-stage Cenozoic collision between India and Asia. *Proceedings of the National Academy of Sciences*, *109*(20), 7659–7664. https://doi.org/10.1073/pnas.1117262109

Van Hinsbergen, D. J. J., Lippert, P. C., Li, S., Huang, W., Advokaat, E. L., & Spakman, W. (2019). Reconstructing Greater India: Paleogeographic, kinematic, and geodynamic perspectives. *Tectonophysics*, *760*, 69–94. https://doi.org/10.1016/j.tecto.2018.04.006

Van Hinsbergen, D. J. J., Steinberger, B., Doubrovine, P. V., & Gassmöller, R. (2011). Acceleration and deceleration of India-Asia convergence since the Cretaceous: Roles of mantle plumes and continental collision. *Journal of Geophysical Research: Solid Earth*, *116* (B6), B06101. https://doi.org/10.1029/2010JB008051

Ventosa, S., Schimmel, M., & Stutzmann, E. (2019). Towards the processing of large data volumes with phase cross-correlation. *Seismological Research Letters*, *90*(4), 1663–1669. https://doi.org/10.1785/0220190022

Vinnik, L. P., Reigber, C., Aleshin, I. M., Kosarev, G. L., Kaban, M. K., Oreshin, S. I., & Roecker, S. W. (2004). Receiver function tomography of the central Tien Shan. *Earth and Planetary Science Letters*, *225*(1–2), 131–146. https://doi.org/10.1016/j.epsl.2004.05.039

Wallis, D., Phillips, R. J., & Lloyd, G. E. (2014). Evolution of the Eastern Karakoram Metamorphic Complex, Ladakh, NW India, and its relationship to magmatism and regional tectonics. *Tectonophysics*, *626*, 41–52. https://doi.org/10.1016/j.tecto.2014.03.023

Wang, Q., Hawkesworth, C. J., Wyman, D., Chung, S. L., Wu, F. Y., Li, X. H., et al. (2016). Pliocene-Quaternary crustal melting in central and northern Tibet and insights into crustal flow. *Nature Communications*, *7*(1), 1–11. https://doi.org/10.1038/ncomms11888

Wapenaar, K. (2004). Retrieving the elastodynamic Green's function of an arbitrary inhomogeneous medium by cross-correlation. *Physical Review Letters*, *93*(25), 254301. https://doi.org/10.1103/PhysRevLett.93.254301

Wessel, P., Smith, W. H., Scharroo, R., Luis, J., & Wobbe, F. (2013). Generic mapping tools: Improved version released. *Eos, Transactions American Geophysical Union*, *94*(45), 409–410. https://doi.org/10.1002/2013EO450001

Westaway, R. (1995). Crustal volume balance during the India-Eurasia collision and altitude of the Tibetan Plateau: A working hypothesis. *Journal of Geophysical Research: Solid Earth*, *100*(B8), 15173–15192. https://doi.org/10.1029/95JB01310

Wittlinger, G., Farra, V., Hetényi, G., Vergne, J., & Nábělek, J. (2009). Seismic velocities in southern Tibet lower crust: A receiver function approach for eclogite detection. *Geophysical Journal International*, *177*(3), 1037–1049. https://doi.org/10.1111/j.1365-246X.2008.04084.x

Wittlinger, G., Vergne, J., Tapponnier, P., Farra, V., Poupinet, G., Jiang, M., et al. (2004). Teleseismic imaging of subducting lithosphere and Moho offsets beneath western Tibet. *Earth and Planetary Science Letters*, *221*(1–4), 117–130. https://doi.org/10.1016/S0012-821X(03)00723-4

Xu, Q., Zhao, J., Yuan, X., Liu, H., Ju, C., Schurr, B., & Bloch, W. (2021). Deep crustal contact between the Pamir and Tarim Basin deduced from receiver functions. *Geophysical Research Letters*, *48*(9), e2021GL093271. https://doi.org/10.1029/2021GL093271

Xu, Q., Zhao, J., Yuan, X., Liu, H., & Pei, S. (2017). Detailed configuration of the underthrusting Indian lithosphere beneath western Tibet revealed by receiver function images. *Journal of Geophysical Research: Solid Earth*, *122*(10), 8257–8269. https://doi.org/10.1002/2017JB014490

Xu, Z. J., Song, X., & Zhu, L. (2013). Crustal and uppermost mantle S velocity structure under Hi-CLIMB seismic array in central Tibetan Plateau from joint inversion of surface wave dispersion and receiver function data. *Tectonophysics*, *584*, 209–220. https://doi.org/10.1016/j.tecto.2012.08.024

Yang, Y., Ritzwoller, M. H., Zheng, Y., Shen, W., Levshin, A. L., & Xie, Z. (2012). A synoptic view of the distribution and connectivity of the mid-crustal low-velocity zone beneath Tibet. *Journal of Geophysical Research: Solid Earth*, *117*(B4), B04303. https://doi.org/10.1029/2011JB008810

Yang, Y., Zheng, Y., Chen, J., Zhou, S., Celyan, S., Sandvol, E., et al. (2010). Rayleigh wave phase velocity maps of Tibet and the surrounding regions from ambient seismic noise tomography. *Geochemistry, Geophysics, Geosystems*, *11*(8), Q08010. https://doi.org/10.1029/2010GC003119

Yin, A. (2006). Cenozoic tectonic evolution of the Himalayan orogen as constrained by along-strike variation of structural geometry, exhumation history, and foreland sedimentation. *Earth-Science Reviews*, *76*(1–2), 1–131. https://doi.org/10.1016/j.earscirev.2005.05.004

Yin, A., & Harrison, T. M. (2000). Geologic evolution of the Himalayan-Tibetan orogen. *Annual Review of Earth and Planetary Sciences*, *28*(1), 211–280. https://doi.org/10.1146/annurev.earth.28.1.211

Zhang, B., Bao, X., & Xu, Y. (2020). Distinct orogenic processes in the South-and North-Central Tien Shan from receiver functions. *Geophysical Research Letters*, *47*(6), e2019GL086941. https://doi.org/10.1029/2019GL086941

Zhang, P. Z., Shen, Z., Wang, M., Gan, W., Burgmann, R., Molnar, P., et al. (2004). Continuous deformation of the Tibetan Plateau from global positioning system data. *Geology*, *32*(9), 809–812. https://doi.org/10.1130/G20554.1

Zhang, Z., Wang, Y., Houseman, G. A., Xu, T., Wu, Z., Yuan, X., et al. (2014). The Moho beneath western Tibet: Shear zones and eclogitization in the lower crust. *Earth and Planetary Science Letters*, *408*, 370–377. https://doi.org/10.1016/j.epsl.2014.10.022

Zhao, J., Neupane, B., Liu, H., & Yan, D. (2020). Lithospheric structure of western Tibet–A brief review. *Journal of Asian Earth Sciences*, *198*, 104159. https://doi.org/10.1016/j.jseaes.2019.104159

Zhao, J., Yuan, X., Liu, H., Kumar, P., Pei, S., Kind, R., et al. (2010). The boundary between the Indian and Asian tectonic plates below Tibet. *Proceedings of the National Academy of Sciences*, *107*(25), 11229–11233. https://doi.org/10.1073/pnas.1001921107

Zhao, W., Kumar, P., Mechie, J., Kind, R., Meissner, R., Wu, Z., et al. (2011). Tibetan plate overriding the Asian plate in central and northern Tibet. *Nature Geoscience*, *4*(12), 870–873. https://doi.org/10.1038/ngeo1309

Zhu, L., & Helmberger, D. V. (1998). Moho offset across the northern margin of the Tibetan Plateau. *Science*, *281*(5380), 1170–1172. https://doi.org/10.1126/science.281.5380.1170

References From the Supporting Information

Hanna, A. C., & Weeraratne, D. S. (2013). Surface wave velocity structure of the western Himalayan syntaxis. *Geophysical Journal International*, *194*(3), 1866–1877. https://doi.org/10.1093/gji/ggt203

Herrmann, R. B. (2013). Computer programs in seismology: An evolving tool for instruction and research. *Seismological Research Letters*, *84*(6), 1081–1088. https://doi.org/10.1785/0220110096

Oreshin, S., Kiselev, S., Vinnik, L., Prakasam, K. S., Rai, S. S., Makeyeva, L., & Savvin, Y. (2008). Crust and mantle beneath western Himalaya, Ladakh and western Tibet from integrated seismic data. *Earth and Planetary Science Letters*, *271*(1–4), 75–87. https://doi.org/10.1016/j.epsl.2008.03.048

Roecker, S. W. (1982). Velocity structure of the Pamir-Hindu Kush region: Possible evidence of subducted crust. *Journal of Geophysical Research: Solid Earth*, *87*(B2), 945–959. https://doi.org/10.1029/JB087iB02p00945

Yuan, H., & Bodin, T. (2018). A probabilistic shear wave velocity model of the crust in the central West Australian Craton constrained by trans-dimensional inversion of ambient noise dispersion. *Tectonics*, *37*(7), 1994–2012. https://doi.org/10.1029/2017TC004834